Separation and Purification Technology 326 (2023) 124866

Contents lists available at ScienceDirect

Separation and Purification Technology

journal homepage: www.elsevier.com/locate/seppur

Synergistic performance of Ni-Ca based dual functional materials under the coexistence of moisture and oxygen in CO_2 source for integrated carbon capture and utilisation

Xiaotong Zhao [a], Shuzhuang Sun [a], Yingrui Zhang [a], Yuanyuan Wang [a], Yuan Zhu [a], Paul Williams [b,*], Shaoliang Guan [c], Chunfei Wu [a,*]

[a] School of Chemistry and Chemical Engineering, Queen's University Belfast, Belfast BT7 1NN, UK
[b] School of Chemical and Process Engineering University of Leeds, Leeds LS2 9JT, UK
[c] HarwellXPS R92, Research Complex at Harwell, Rutherford Appleton Laboratory, Didcot OX11 0FA, UK

ARTICLE INFO

Keywords:
ICCU-DRM
Flue gas
Dual-functional materials
Dry reforming methane

ABSTRACT

Global warming and climate change require urgent reduction of CO_2 emissions. Integrated carbon capture and utilisation combined with dry reforming of methane (ICCU-DRM) has the potential to mitigate greenhouse gas emissions by capturing and converting CO_2 and CH_4 into valuable syngas. However, the performance and stability of dual-functional materials (DFMs) are unclear under real-world flue gas conditions, particularly in the presence of steam and O_2. In this study, we elucidated the mechanisms of the performance of a $Ni_{0.05}/CaO_{0.95}$ DFM under various flue gas conditions and investigated the combined effects of steam and O_2 on CO_2 uptake, CO and H_2 yields and cyclic stability. Our approach includes the synthesis and evaluation of the DFM using advanced characterisation techniques, such as XRD, in-situ infrared spectroscopy, CH_4-TPR, SEM, EXD, FIB-SEM, BET, and XPS, to gain insights into the properties and behaviour of the DFM under different flue gas conditions. The findings show that under the simulated flue gas condition (10.0 % CO_2 + 6.0 % H_2O + 6.7 % O_2/N_2), there was a significant deterioration in performance, with CO_2 uptake of only 5.7 mmol.g-1, average H_2 yield of 11 mmol.g^{-1} and average CO yield of 6.2 mmol.g^{-1}. While under the ideal condition (10.0 % CO_2/N_2), the CO_2 uptake, average H_2 yield and average CO yield were 10.7 mmol.g^{-1}, 16.9 mmol.g^{-1} and 23.1 mmol.g^{-1}, respectively. FIB-SEM and XPS analysis highlighted the combined effect of steam and O_2 on the performance of $Ni_{0.05}/CaO_{0.95}$ DFM during ICCU-DRM. Notably, the presence of O_2 promoted the oxidation of Ni, resulting in decreased catalytic activity and volumetric expansion of Ni particles. Furthermore, the presence of steam promoted CO_2 adsorption, inducing additional volumetric expansion of the CaO component of DFM. These synergistic expansions form a dense shell on the surface, hindering the reduction of internal NiO, thereby diminishing DFM performance.

1. Introduction

Global warming causes severe weather conditions bringing significant challenges to social and economic development [1]. The large emissions of CO_2 are responsible for global warming. Technologies such as carbon capture and utilisation (CCU) [2,3] and carbon capture and storage (CCS) [4–7] have been intensively developed to reduce carbon emissions. In particular, integrated carbon capture and utilisation (ICCU) [8–11] has been gaining more attention. ICCU combines carbon capture and CO_2 conversion in a single reaction system isothermally by dual functional materials (DFMs), which contain both sorbents for CO_2 capture and catalysts for CO_2 conversion. This technology can directly convert the captured CO_2 into chemicals without transportation and storage of the captured CO_2, as is the case with conventional CO_2 adsorption. In addition, ICCU can occur in one single reactor. Compared with traditional CCU and CCS technologies, ICCU shows the advantages of low energy consumption and low capital investment.

DFMs, acting as combined CO_2 sorbents and catalysts, are fundamental to ICCU technology. Today, extensive research efforts are being poured into enhancing DFM performance. This typically involves

* Corresponding authors.
E-mail addresses: p.t.williams@leeds.ac.uk (P. Williams), c.wu@qub.ac.uk (C. Wu).

https://doi.org/10.1016/j.seppur.2023.124866
Received 21 June 2023; Received in revised form 19 August 2023; Accepted 19 August 2023
Available online 22 August 2023

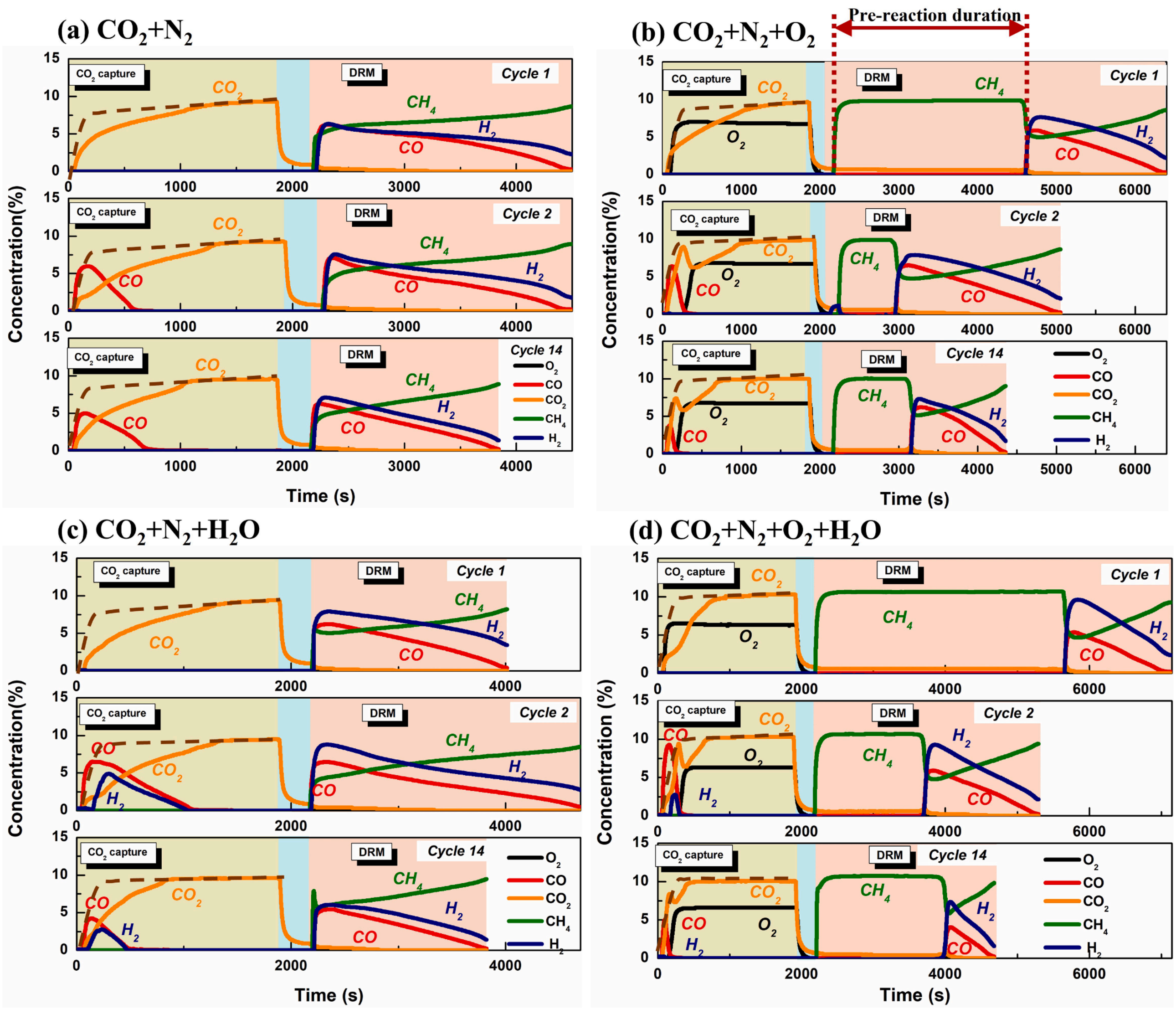

Fig. 1. ICCU-DRM evaluation of cycle 1, cycle 2 and cycle 14 using $Ni_{0.05}/Cao_{0.95}$ under (a) ideal condition (10.0 % CO_2/N_2); (b) O_2-containing condition (10.0 % CO_2 + 6.0 % H_2O/N_2); (c) Steam-containing condition (10.0 % CO_2 + 6.7 % O_2/N_2) and (d) Simulated flue gas condition (10.0 % CO_2 + 6.0 % H_2O + 6.7 % O_2/N_2).

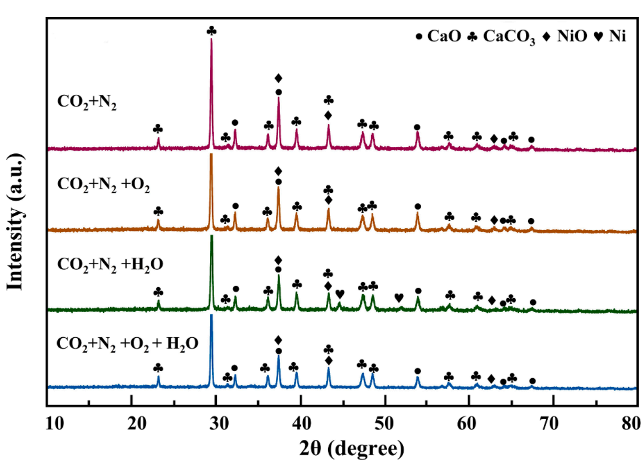

Fig. 2. XRD spectra of adsorbed samples under different flue gas conditions.

incorporating metal additives, as well as fine-tuning the distribution of catalysts and adsorbents [12]. For instance, a study demonstrated that a Ni/CaO DFM, when infused with metal oxides, exhibited impressive performance for CO_2 capture and conversion. Of the variations tested, the one doped with ZrO_2 delivered the top performance [13]. Moreover, research has shown that introducing CeO_2 into CaO-based DFMs can substantially boost their cycle stabilities [14,15]. It has also been observed that doping with CeO_2 can even improve CO_2 conversion rates [16]. Recently, a Ca-Fe bifunctional material was reported, which uses CaO for CO_2 capture and Fe as an oxygen carrier for conversion. By optimising the composition, a Ca-Fe DFM containing 27% Iron exhibited robust stability and CO yield over 10 cycles, without deactivation [17]. Apart from utilising additives and optimising proportions, scientists are also investigating new preparation methods to enhance DFM performance [18,19]. Techniques like co-precipitation [20] and sol–gel [21] can help fine-tune the morphology of the DFMs, porosity, and particle size, thereby augmenting their CO_2 adsorption capabilities. There are also several innovative research projects aimed at creating novel DFMs that are different from conventional CaO-based DFMs. For example, some researchers used DRIFTS-MS to study the capture and conversion mechanisms of a NiRu–Na_2O DFM in CO_2 methanation [22]. These studies offered insight into adjusting catalyst-adsorbent interfaces, adsorption strength, and site distributions for DFMs optimisation. On another front, a Ru/K_2CO_3–MgO DFM was engineered for low-temperature CO_2 capture and methanation, and the optimised

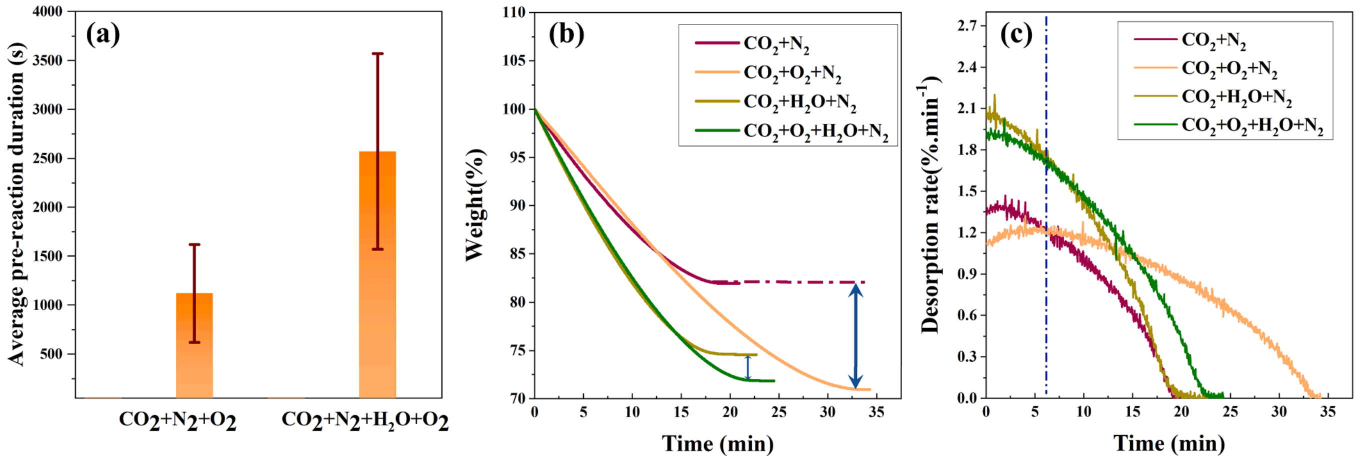

Fig. 3. Average Pre-reaction duration of 14 cycles under the four different flue gas conditions (e), TG curve (f) and TPR rate by 10.0 % CH_4/N_2 of $Ni_{0.05}CaO_{0.95}$ with the temperature kept at 650 °C isothermally under atmospheric pressure and flow rate of 100 mL min^{-1}.

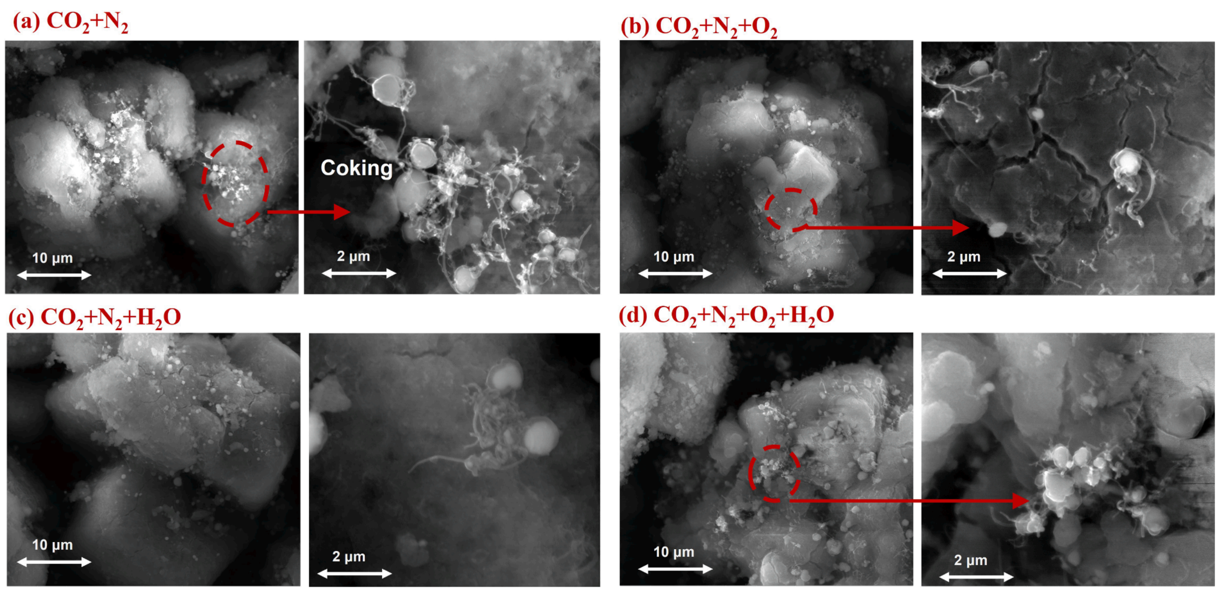

Fig. 4. The coke on DFM after cycling under (a) ideal condition (10.0 % CO_2/N_2); (b) O_2-containing condition (10.0 % CO_2 + 6.0 % H_2O/N_2); (c) Steam-containing condition (10.0 % CO_2 + 6.7 % O_2/N_2) and (d) Simulated flue gas condition (10.0 % CO_2 + 6.0 % H_2O + 6.7 % O_2/N_2).

material demonstrated stable Methane yields over multiple cycles [23]. Some scientists also used PEI to capture CO_2, forming carbamic acid salts. Under the influence of a Rh catalyst, these salts were hydrogenated to generate formate esters [24]. In essence, these pioneering studies offer various preparation strategies for DFMs that can guide their design for more effective ICCU.

In the realm of CO_2 conversion techniques, dry reforming of methane (DRM) has emerged as a promising approach to utilise CO_2 for syngas production (Eq. (1). DRM can aid in reducing CH_4, a potent greenhouse gas with a global warming potential per molecule around 30 times that of CO_2 [25]. Consequently, integrating ICCU and DRM into a single process (ICCU-DRM) is an attractive proposition to limit CO_2 emissions from flue gas. However, catalysts employed in DRM frequently face the issue of coke deposition, which tends to diminish their catalytic performance [26]. Multiple studies are, therefore, focused on augmenting the resistance to coking and enhancing catalyst stability [27]. For instance, one research identified a Rh-Ni bimetallic catalyst that improves coking resistance by balancing methane dissociation and CO_2 activation [28]. Other researchers synthesised a Ru/CeO_2 catalyst as a part of DRM, demonstrating that Ru and CeO_2 worked in synergy to promote coking resistance and catalytic performance [29,30]. Interestingly, the ICCU-DRM process offers a unique solution to the coking issue during the CO_2 capture phase. The coke produced by DRM can be consumed through a reverse Boudouard reaction when it reacts with CO_2 [31,32] (Eq. (2). Therefore, the challenges associated with developing and modifying DFMs for ICCU-DRM might be distinct from traditional DRM. Despite its potential, very few studies target ICCU-DRM in their DFM research. As ICCU is a relatively nascent technology, the bulk of research has been concentrated on reverse water–gas shift (RWGS) and methanation. The complexity of ICCU-DRM also implies that related research is not yet comprehensive. However, recent studies are beginning to address this knowledge gap. One study used limestone-derived CaO as the CO_2 sorbent and Ni supported on $MgO-Al_2O_3$, derived from a hydrotalcite precursor, as the DRM catalyst [33]. To enhance DFM performance in ICCU-DRM, a study employed N_2-doped porous carbon materials derived from biomass, revealing key insights into material properties necessary for effective CO_2 adsorption and DRM catalysis [34]. Another study explored the synergistic effects of Ni-CaO DFMs in ICCU. By optimising the dispersion of Ni nanoparticles on a CaO carrier, impressive conversion efficiencies of 96.5 %

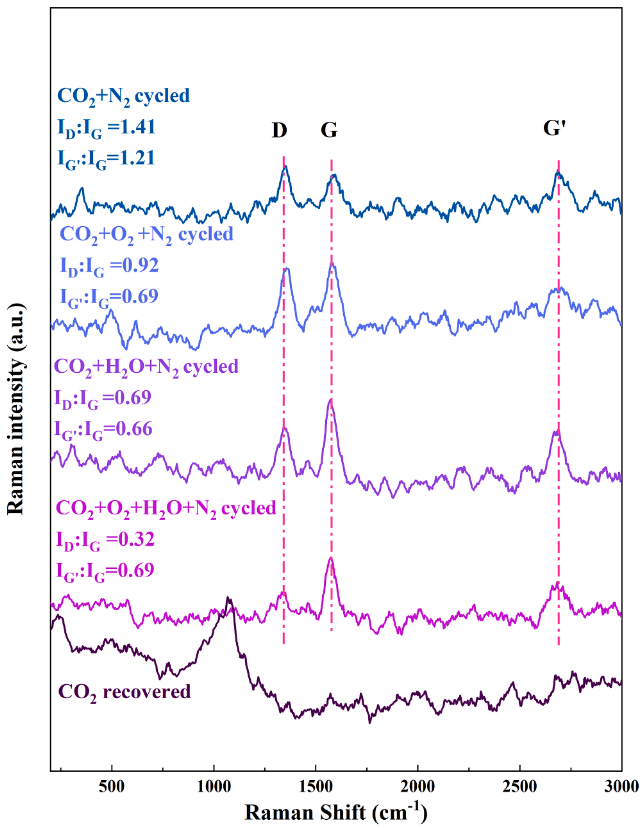

Fig. 5. Raman spectrums of $Ni_{0.05}CaO_{0.95}$ cycled under ideal condition (10.0 % CO_2/N_2), O_2-containing condition (10.0 % CO_2 + 6.0 % H_2O/N_2), steam-containing condition (10.0 % CO_2 + 6.7 % O_2/N_2), simulated flue gas condition (10.0 % CO_2 + 6.0 % H_2O + 6.7 % O_2/N_2) and cycled then recovered by CO_2 under under ideal condition.

for CO_2 and 96.0 % for CH_4 were achieved [35].

$$CH_4 + CO_2 = 2CO + 2H_2 \tag{1}$$

$$C + CO_2 = 2CO \tag{2}$$

However, most of the research conducted so far has tested flue gas conditions containing only CO_2 and inert gas, typically N_2. This does not align with real-world scenarios. Flue gases from power or cement plants often contain O_2 and steam. Therefore, a comprehensive understanding of the roles of O_2 and steam in this procedure is urgently required. Recently, a study by Alejandro and his team highlighted the adverse impact of oxidising species on the performance of a DFM composed of 4% Ru-8% Na_2CO_3-8% CaO/Al_2O_3 [36]. Simultaneously, steam has been shown to boost the CO_2 capacity of CaO-based DFMs [37]. However, the overall impact of O_2 and steam on the industrial ICCU-DRM process remains unclear. From a practical and industrial viewpoint, it would be advantageous to sidestep the additional costs tied to the removal of steam and O_2 from the flue gas. Therefore, our approach should lean towards the development of DFMs that can maintain superior performance and stability in conditions containing steam and O_2. The first step in this journey is to discern the impact of steam and O_2 on DFM performance and stability. A critical area of focus should be the cyclical stability of DFMs under flue gas conditions that contain O_2 and steam. Addressing this pressing issue calls for extensive experimental investigations to thoroughly understand these effects. The knowledge gleaned from such explorations will then serve as a foundation for suggesting modifications and optimising the performance of DFMs in flue gas conditions that include O_2 and steam.

Ni-CaO based DFMs have significant potential for widespread use in large-scale industrial applications [38] to explore the impact of steam and O_2 in flue gas on its performance. Therefore, we developed a $Ni_{0.05}/CaO_{0.95}$ DFM and assessed its efficiency in the ICCU-DRM process under flue gas conditions. These conditions encompassed an ideal condition (10% CO_2/N_2), a steam-containing condition (10.0% CO_2 + 6.0% H_2O/N_2), an O_2-containing condition (10.0% CO_2 + 6.7% O_2/N_2), and a simulated flue gas condition (10.0% CO_2 + 6.0% H_2O + 6.7% O_2/N_2). Our in-depth analysis aimed to understand the effects of steam and O_2 on the stability of DFMs during ICCU-DRM operations. A special emphasis is placed on how O_2 and steam jointly impact CO_2 absorption, CO and H_2 yields, and cyclic stability.

2. Experimental section

2.1. Synthesis of dual functional material (DFM)

Choosing the appropriate DFMs for ICCU-DRM requires a balance between performance and economic feasibility. While certain noble metal catalysts such as Ru, Rh, and Pd showcase exceptional catalytic performance, their high cost necessitates a more economical alternative for large-scale applications. Ni, due to its affordability, has emerged as the most economically viable choice, making it the front-runner for widespread adoption [39,40]. Hence, Ni-CaO DFMs have promising industrial applicability, thereby $Ni_{0.05}/Cao_{0.95}$ was synthesised as the DFM by the wet impregnation method. Specifically, $Ni(NO_3)_2{\cdot}6H_2O$ (Sigma-Aldrich, >99.0 %) and $Ca(NO_3)_2{\cdot}6H_2O$ (Sigma-Aldrich, >99.0 %) were dissolved into distilled water with constant stirring at room temperature for 1 h. The mole ratio was: Ni_2^+: Ca_2^+: H_2O = 0.05: 0.95: 400. Subsequently, the solution was evaporated with stirring at 95 ℃ and then dried in a Muffle furnace at 130 ℃ for 12 h. After drying, the material was then ground into powder and calcined in still air in the Muffle furnace with the heating program of 5 ℃ min^{-1} to 750 ℃ for 3 h to obtain the original $Ni_{0.05}/Cao_{0.95}$. Then it was reduced at 700 ℃ for 1 h in 100 mL min^{-1} 5.0 % H_2/Ar to obtain reduced $Ni_{0.05}/Cao_{0.95}$ DFM.

2.2. Material characterisation

The phase information of the adsorbed samples under the four different flue gas conditions was determined using powder X-ray diffraction (XRD) on a PANalytical Empyrean series two diffractometer system equipped with a Cu Kα X-ray source (2 Theta = 5–80°) The in-situ infrared spectroscopy was used to investigate the decomposition of $CaCO_3$ under CH_4 and its subsequent CO_2 re-adsorption. Initially, the DFM sample, fully adsorbed under ideal conditions (10% CO_2/N_2), was placed in the sample holder. The sample was then purged with N_2 for 10 min, followed by the introduction of a 10% CH_4/N_2 mixture for 30 min. Afterwards, the sample was purged again with N_2 for 10 min, and finally, a gas mixture containing 10% CO_2/N_2 was introduced for adsorption. Throughout the experiment, the temperature was maintained at 650 °C, and the gas flow rate was set at 100 mL.min^{-1}. The CH_4 temperature programmed reduction (CH_4-TPR) curve was obtained using a Hi-Res TGA 2950 thermogravimetric analyser. The $Ni_{0.05}/CaO_{0.95}$ DFM was pretreated at 650 °C for 10 min in an N_2 atmosphere. Subsequently, a 10.0% CH_4/N_2 mixture was introduced, and the process continued until no further decrease in weight was observed, indicating equilibrium had been reached. A FEI Helios G4 CX Dual Beam high resolution monochromate field emission gun (FEG) scanning electron microscope (SEM) with a precise focused ion beam (FIB) was employed to obtain cross-sectional images of the samples. Energy-dispersive X-ray spectroscopy (EDX) was used to analyse the elemental distribution within the samples. The surface area and pore diameter were calculated using the Brunauer-Emmett-Teller (BET) method and the desorption isotherm branch, respectively. Lastly, the X-ray photoelectron spectrum (XPS) analysis was conducted on a Thermo Fisher Scientific NEXSA spectrometer to further characterise the samples.

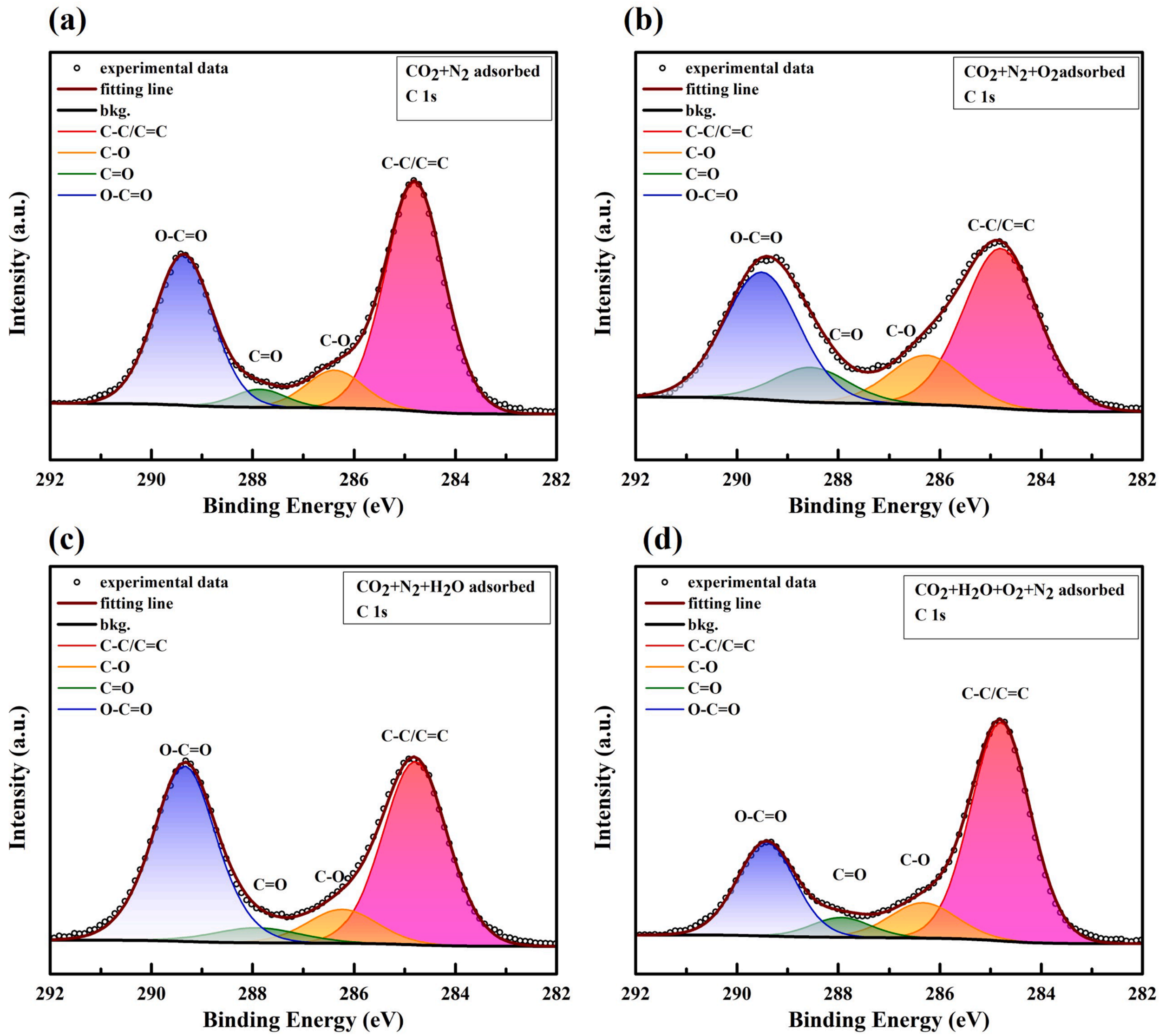

Fig. 6. XPS analysis of C 1 s region of $Ni_{0.05}/CaO_{0.95}$ after adsorption under (a) ideal condition (10.0 % CO_2/N_2); (b) O_2-containing condition (10.0 % CO_2 + 6.0 % H_2O/N_2); (c) Steam-containing condition (10.0 % CO_2 + 6.7 % O_2/N_2) and (d) Simulated flue gas condition (10.0 % CO_2 + 6.0 % H_2O + 6.7 % O_2/N_2).

2.3. ICCU-DRM procedure

The experimental setup is shown in Fig. S1, which is similar to our previous report [40]. The ICCU-DRM evaluations of $Ni_{0.05}/Cao_{0.95}$ DFM were conducted in a quartz reaction tube (OD: 12.0 mm; ID: 10.5 mm; L: 65.0 cm). The quartz tube was fixed in the middle of a tube furnace (Elite TSH 12/50/300-2416CG) for heating. The 0.30 g of $Ni_{0.05}/Cao_{0.95}$ DFM which was fixed by quartz wool, was placed in the centre of the quartz tube. A thermocouple was placed in the same position as the sample to monitor the temperature. The inlet gases (CO_2, N_2, air) were controlled by mass flowmeters (OMEGA FMA-A2306). The mass flowmeters were calibrated by a bubble flowmeter. Steam was generated by introducing water using a water pump. The outlet gases were analysed by a flue gas analyser system, which included a flue gas analyser (Enerac 700 AV; NDIR detector) and an H_2 analyser (CX-02; TCD detector).

The ICCU-DRM evaluations were conducted at ideal condition (10 % CO_2/N_2), steam-containing condition (10.0% CO_2 + 6.0% H_2O/N_2), O_2-containing condition (10.0% CO_2 + 6.7% O_2/N_2) and simulated power plant flue gas condition (10.0% CO_2 + 6.0% H_2O + 6.7% O_2/N_2) respectively. For each condition, 14 ICCU-DRM cycles were conducted to observe the stability and performance of $Ni_{0.05}/Cao_{0.95}$ under different flue gas conditions. The flow rates of inlet gas were all kept at 100 mL.min^{-1} while assuming that the flow rates of outlet gas were the same. For a typical cycle, during the CO_2 capture stage, the simulated flue gases were introduced for 30 mins, and then the reaction tube was purged by N_2 for 5 mins. For the DRM stage, the 10.0 % CH_4/N_2 was introduced until the CO concentration shown on the analyser was below 0.05 %. Then the simulated gases were introduced again to conduct the next cycle after purging by N_2 for 5 mins. The temperature was kept at 650 ℃ before finishing the 14th cycle. The ICCU-DRM performance was evaluated by the real-time signals of CH_4, H_2, CO and CO_2.

3. Results and discussions

3.1. $Ni_{0.05}/Cao_{0.95}$ performance for ICCU-DRM under different flue gas conditions

3.1.1. Influence of H_2O and O_2 presence on CO_2 capture performance during ICCU-DRM

Fig. 1 presents the real-time assessment of ICCU-DRM over cycles 1, 2, and 14, employing $Ni_{0.05}/Cao_{0.95}$ under four distinct flue gas conditions, including ideal condition (10.0 % CO_2/N_2), O_2-containing condition (10.0 % CO_2 + 6.0 % H_2O/N_2), steam-containing condition (10.0 % CO_2 + 6.7 % O_2/N_2), and simulated flue gas condition (10.0 % CO_2 +

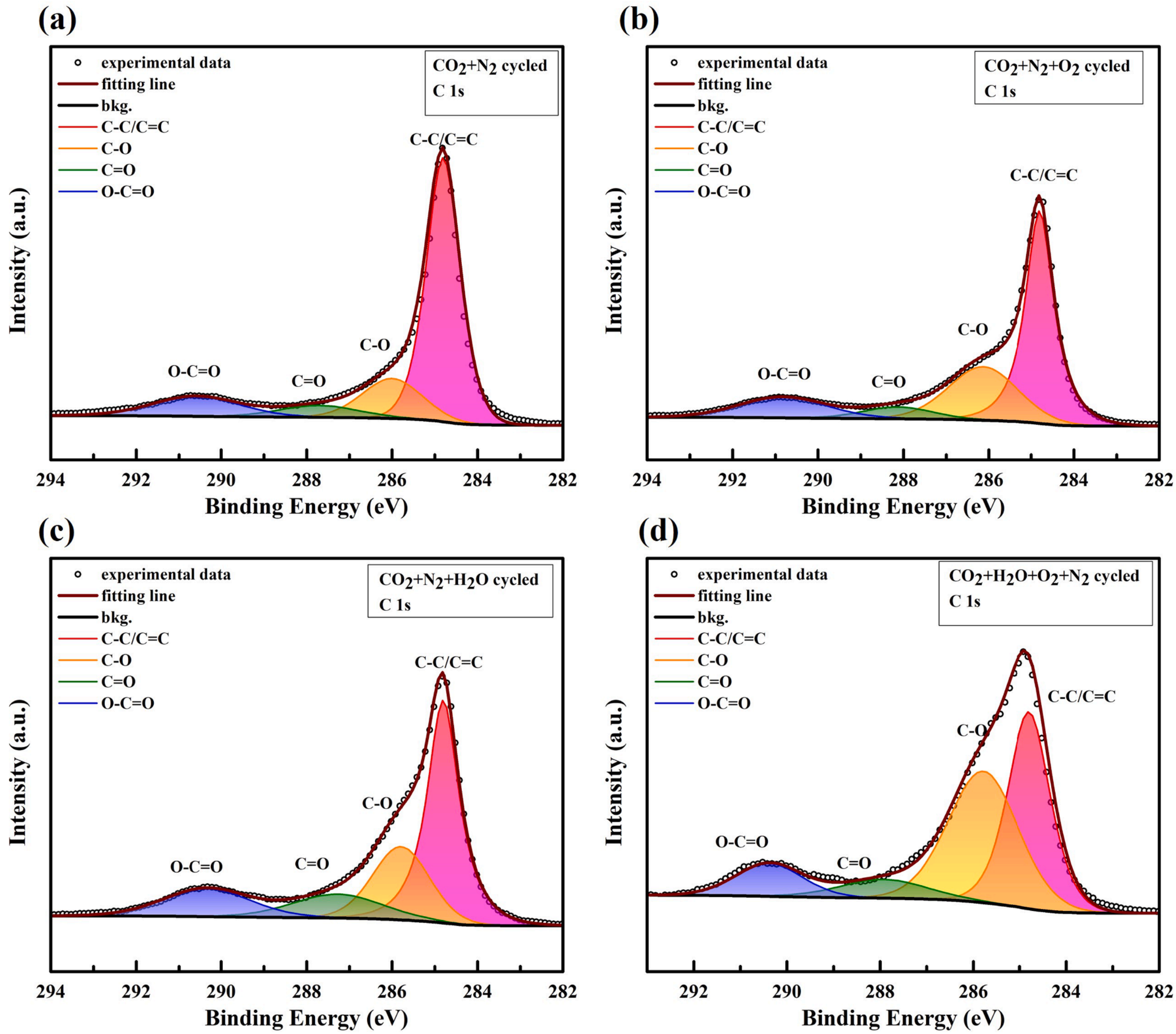

Fig. 7. XPS analysis of C 1 s region of $Ni_{0.05}/CaO_{0.95}$ after 14 cycles under (a) ideal condition (10.0 % CO_2/N_2); (b) O_2-containing condition (10.0 % CO_2 + 6.0 % H_2O/N_2); (c) Steam-containing condition (10.0 % CO_2 + 6.7 % O_2/N_2) and (d) Simulated flue gas condition (10.0 % CO_2 + 6.0 % H_2O + 6.7 % O_2/N_2).

6.0 % H_2O + 6.7 % O_2/N_2). As demonstrated in Fig. 1 (a), during the initial cycle, the gradual increase in CO_2 concentration from 0% to 10% signifies the adsorption of CO_2 by CaO. Following a 5-minute purge with N_2, 10% of CH_4 was introduced to commence the DRM reaction. As shown in Fig. 1 (a), starting from the second cycle, CO is generated during the CO_2 capture stage, with the concentration rapidly rising to 5.5% and then gradually decreasing to 0 % over the next approximately 600 s. Considering that the concentration of CO in the CO_2 capture stage of the first cycle is only 0.01 %, the generation of CO during the carbon capture stage is neglected. Therefore, it is plausible to exclude the possibility of CO_2 decomposition generating CO. In fact, the amount of CO generated from the thermal decomposition of CO_2 at lower concentrations using Ni-based catalysts is quite limited [41]. It often requires the aid of means such as plasma to achieve a considerable yield of CO by CO_2 pyrolysis [42]. Therefore, the main reason for the generation of CO should be related to the coke formed on the DFM surface during the previous cycle, which reacted with CO_2 through the reverse Boudouard reaction (Eq. (2)) [31].

Under O_2-containing conditions, as depicted in Fig. 1 (b), due to the reaction between coke and O_2 [40,43], the duration of the appearance of CO was only about 300 s which was much shorter compared to that under ideal conditions (600 s). Meanwhile, the O_2 generation was delayed by about 200 s during the second cycle, suggesting that O_2 was involved in the reaction with coke. Concurrently, the CO_2 curve exhibited a period of fluctuation. This could be attributed to the additional generation of CO_2 resulting from the reaction between O_2 and coke [44], causing a rapid rise of concentration from 0 % to 9.8 % in the CO_2 curve, while the continuous adsorption of CO_2 by CaO led to a decrease in its concentration to about 5.0 % as the coke was consumed by the reverse Boudouard reaction (Eq. (2)) [40]. As shown in Fig. 1 (c), under the steam-containing condition, H_2 production was observed during the CO_2 capture stage. The highest concentration was at around 4.0 %. This could be ascribed to the carbon steam gasification (CSG) reaction between coke and steam (Eq. (3)) [45]. Under simulated flue gas conditions containing both O_2 and steam, like Fig. 1 (b), the duration of CO presence significantly decreased, only lasting for approximately 300 s. Meanwhile, the duration of H_2 appearance also noticeably reduced, lasting for about 50 s and with the highest concentration reaching only 2.5%. This indicates that the reaction between O_2 and coke predominantly occurs during the CO_2 capture stage, thereby reducing the reverse Boudouard reaction and CSG reaction.

$$C + H_2O = CO + H_2 \tag{3}$$

Table 1
Summary of atomic ratio of C 1 s by XPS analysis.

Sample	Name	Peak BE	Atomic %
A1	C–C/C=C	284.8	53.06
	C-O	286.38	8.52
	C=O	287.86	3.67
	O–C=O	289.37	34.75
A2	C–C/C=C	284.8	43.00
	C-O	286.27	13.25
	C=O	288.53	9.38
	O–C=O	289.51	34.37
A3	C–C/C=C	284.8	43.97
	C-O	286.23	8.81
	C=O	287.91	4.80
	O–C=O	289.34	42.42
A4	C–C/C=C	284.8	59.27
	C-O	286.33	10.78
	C=O	287.94	5.29
	O–C=O	289.42	24.66
C1	C–C/C=C	284.8	64.67
	C-O	286	16.54
	C=O	287.71	6.54
	O–C=O	290.6	12.25
C2	C–C/C=C	284.8	52.88
	C-O	286.13	27.46
	C=O	288.13	6.11
	O–C=O	290.83	13.55
C3	C–C/C=C	284.8	49.03
	C-O	285.79	24.15
	C=O	287.27	12.45
	O–C=O	290.35	14.38
C4	C–C/C=C	284.8	39.95
	C-O	285.79	42.45
	C=O	287.92	7.49
	O–C=O	290.39	10.11

A1: $Ni_{0.05}/CaO_{0.95}$ adsorbed under ideal condition (10% CO_2/N_2).
A2: $Ni_{0.05}/CaO_{0.95}$ adsorbed under O_2-containing condition (10.0 % CO_2 + 6.0 % H_2O/N_2).
A3: $Ni_{0.05}/CaO_{0.95}$ adsorbed under steam-containing condition (10.0 % CO_2 + 6.7 % O_2/N_2).
A4: $Ni_{0.05}/CaO_{0.95}$ adsorbed under simulated flue gas condition (10.0 % CO_2 + 6.0 % H_2O + 6.7 % O_2/N_2).
C1: $Ni_{0.05}/CaO_{0.95}$ regenerated after 14 cycles under ideal condition.
C2: $Ni_{0.05}/CaO_{0.95}$ regenerated after 14 cycles under O_2-containing condition.
C3: $Ni_{0.05}/CaO_{0.95}$ regenerated after 14 cycles under steam-containing condition.
C4: $Ni_{0.05}/CaO_{0.95}$ regenerated after 14 cycles under simulated flue gas condition.

3.1.2. *Influence of H_2O and O_2 presence on CO_2 conversion during ICCU-DRM*

In the DRM process, the equality of H_2 and CO concentrations indicates the equilibrium of the DRM reactions [46]. For the ideal conditions of the 1st cycle, the concentrations of CO and H_2 were nearly equal, at around 5.0 %-6.0 % from 2180 s to 3200 s. Subsequently, the concentration of H_2 surpassed that of CO at around 3200 s. The DRM process comprises two simplified parallel reactions: the decomposition of CH_4 (Eq. (4)), and the reverse Boudouard reaction (Eq. (2)) [47]. The observed increase in H_2 concentration relative to CO indicates an imbalance between the cracking of CH_4 and the consumption of coke by CO_2 [48], leading to coke deposition. As $CaCO_3$ continuously decomposes, the remaining amount of $CaCO_3$ decreases, leading to reduced production of CO_2. This reduced CO_2 availability, in turn, limits the oxidation of coke formed from CH_4 cracking via reverse Boudouard reaction (Eq. (2)). Consequently, coke accumulated on the Ni surface [49,50]. Under the ideal condition, the CO:H_2 ratio for each cycle can be maintained between 1.0 and 1.3, indicating that such conditions favor the balanced progression of the DRM reaction for $Ni_{0.05}CaO_{0.95}$. However, under the O_2-containing condition, as depicted in Fig. 1 (b), the two concentration curves diverge from the very first cycle. Specifically, the highest H_2 concentration reached 7.5%, whereas the peak CO concentration was only 5.0%. This discrepancy is due to the un-reduced state of NiO after O_2 oxidation, which impedes the catalytic activity for the reverse Boudouard reaction of Ni [51–53]. As a result, this oxidation of Ni leads to a decline in the reverse Boudouard reaction during the hydrogenation processes.

As shown in Fig. 2, the peak at around 38°, 43° and 63° correspond to NiO [54]. Ni is highly susceptible to oxidation, even in the absence of O_2 in the flue gas; almost all Ni species are oxidised due to the exposure to air, making Ni difficult to detect by XRD (Fig. 2). Therefore, during the CO_2 capture stage in the presence of O_2, Ni particles undergo oxidation and lose catalytic activity [55]. As a result, NiO needs to be reduced by CH_4 during the CO_2 conversion stage of ICCU. Therefore, a certain period for pre-reduction of NiO is needed during the DRM stage [40], as shown in both Fig. 1 (b) and (d), where the concentration of CH_4 remained at 10.0% for a specific period. As shown in Fig. 1 (c), in the case of steam-containing condition, in the first cycle, the highest concentration of H_2 was 8.0 %, while the highest concentration of CO was 6.0 %. Since this was the initial cycle, the reason for the higher H_2 concentration than CO concentration was not due to catalyst performance degradation. Instead, it could be attributed to the steam adsorbed by the DFM during the CO_2 capture stage, which led to additional H_2 production through a side reaction with CH_4 via the steam methane reforming (SMR) reaction (Eq. (5)) [56]. Fig. 1 (d) demonstrates that under the simulated-flue gas condition, the concentration gap between H_2 and CO has widened further. In the first cycle, the highest H_2 concentration reached 9.6%, while the highest CO concentration was 4.9%. The possible reason could be attributed to the combined effects of catalyst performance deterioration and the occurrence of a side reaction of SMR.

$$CH_4 = C + 2H_2 \tag{4}$$

$$CH_4 + H_2O = CO + 3H_2 \tag{5}$$

Fig. 3 (a) illustrates the average pre-reduction duration of 14 cycles under four distinct types of flue gas conditions. Under the O_2-containing condition, the average pre-reaction duration for 14 cycles was 1100 s, while in the steam-containing condition, the average pre-reaction duration was 2500 s. The coexistence of steam and O_2 significantly prolonged the pre-reduction duration in comparison to the scenario with O_2 only. The prolonged pre-reduction duration implies that steam can function as a hindrance to the reduction of Ni. The prolonging effect of steam on the pre-reaction duration is directly related to the influence of steam on the catalyst performance. We will elucidate their connection and explain the underlying mechanism in the subsequent text.

To investigate the effects of O_2 and steam in flue gas on the DRM process, CH_4-TPR tests were performed on fully adsorbed samples under four different flue gas conditions. As depicted in Fig. 3 (b), the weight of the fully adsorbed samples under ideal conditions decreased from 100% to 82.5% after complete reduction with CH_4. In contrast, under O_2-containing conditions, the weight percentage of the fully adsorbed sample ultimately dropped to 71%, attributable to the reduction of NiO causing greater weight loss. Under steam-containing conditions, the sample weight declined to 74%, significantly lower than under ideal conditions. The additional weight loss can be attributed to the decomposition of $CaCO_3$, indicating a higher $CaCO_3$ percentage in samples under this condition. This observation emphasises the positive impact of steam on the adsorption performance of DFMs [57]. Under the ideal

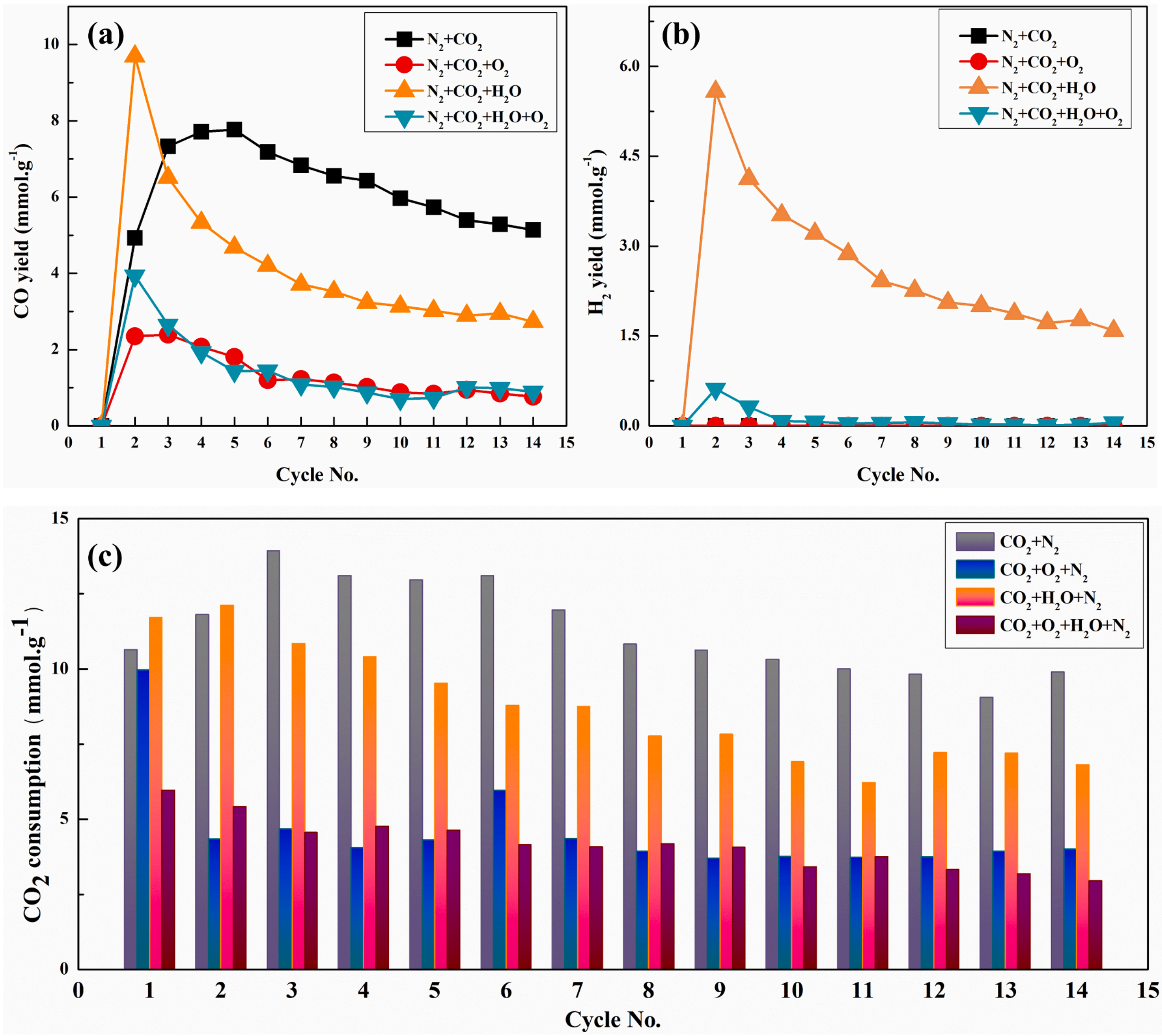

Fig. 8. Yield of CO (a) and H_2 (b) during the CO_2 Capture stage and the CO_2 consumption during each cycle (c).

condition, the final weight percentage was 72%, similar to the O_2-containing condition but lower than the steam-containing condition. Fig. 3 (c) displays the desorption rates of the samples. For conditions containing steam (steam-containing and simulated flue gas conditions), the initial desorption rate was around 2 %.min^{-1}. In conditions without steam (ideal and O_2-containing conditions), the initial desorption rate was only around 1.25 %.min^{-1}. The higher desorption rate suggests that steam can affect the $CaCO_3$ structure [58], facilitating its decomposition. In the first 5 min, the desorption rate of the samples adsorbed under conditions without O_2 (ideal and steam-containing conditions) was slightly higher than those with O_2 (O_2-containing and simulated flue gas conditions). The lower catalytic performance of DFM under O_2-containing conditions might be due to the oxidation of Ni to NiO. Notably, the catalytic activity of NiO was poor for the DRM process [40]. Therefore, it illustrates that elemental Ni plays a key role in this process.

3.1.3. Influence of H_2O and O_2 presence on coke formation in ICCU-DRM

During the catalytic DRM reactions, coking is nearly inevitable [49,59]. As illustrated in Fig. 4, after the DRM reaction, the coke formed on the surface of the Ni can be visualised by SEM. Fig. 5 shows the Raman spectrums of the DFMs cycled under the four flue gas conditions. Three key bands differentiate these species based on their varying degrees of order: the D band, G band, and G' band. The D band, which is approximately at 1350 cm^{-1}, corresponds to amorphous or disordered carbon [60]. The G band, around 1586 cm^{-1}, is related to the sp2 stretching vibration of graphitic carbon [61]. The G' band which is at around 2679 cm^{-1} is linked to the second-order scattering of two phonons [62]. Under the ideal conditions, the intensity ratio I_D:I_G is 1.41 and the I_G:$I_{G'}$ is 1.21. A I_G:$I_{G'}$ ratio >1 typically suggests the formation of a single-layer coke structure. However, under O_2-containing conditions, the I_D:I_G ratio decreases to 0.92, and I_G:$I_{G'}$ reduces to 0.69, which is less than 1, implying a multi-layered coke structure [63]. With the addition of steam only in flue gas (steam-containing condition), the I_D:I_G ratio further decreases to 0.69, while the I_G:$I_{G'}$ ratio is 0.66. Under the simulated flue gas conditions, the I_D:I_G ratio is the lowest among all groups at 0.32, with the I_G:$I_{G'}$ ratio maintained at 0.69. This suggests that the DFM, during the CO_2 capture stage, when adsorbing flue gas containing steam or O_2, tends to facilitate the formation of coke with a higher degree of structural order. Moreover, the coke formed under these conditions typically exhibits a multi-layered structure [64].

As shown in Fig. 5, no carbon-related peaks are detected in the samples post CO_2 reduction, suggesting that the majority of the accumulated carbon is consumed during the CO_2 capture stage. This observation aligns well with findings from previous research [31,40,54]. Consequently, in ICCU-DRM, the catalyst performance degradation issue caused by coke deposition can be addressed. However, with the increase

Table 2
Summary of CO_2 consumptions, CO yields and H_2 yields during the CO_2 capture stage under ideal condition (10.0 % CO_2/N_2), O_2-containing condition (10.0 % CO_2 + 6.0 % H_2O/N_2), steam-containing condition (10.0 % CO_2 + 6.7 % O_2/N_2) and simulated flue gas condition (10.0 % CO_2 + 6.0 % H_2O + 6.7 % O_2/N_2) of 14 cycles.

$CO_2 + N_2$				$CO_2 + H_2O + N_2$			
Cycle No.	CO_2 consumption (mmol. g^{-1})	CO yield (mmol. g^{-1})	H_2 yield (mmol. g^{-1})	Cycle No.	CO_2 consumption (mmol. g^{-1})	CO yield (mmol. g^{-1})	H_2 yield (mmol. g^{-1})
1	10.63	0.00	0.00	1	11.71	0.00	0.00
2	11.81	4.92	0.00	2	12.11	9.70	5.58
3	13.92	7.33	0.00	3	10.83	6.51	4.12
4	13.10	7.71	0.00	4	10.40	5.33	3.52
5	12.95	7.76	0.00	5	9.51	4.68	3.21
6	13.11	7.19	0.00	6	8.77	4.20	2.87
7	11.95	6.83	0.00	7	8.75	3.71	2.41
8	8.82	6.55	0.00	8	7.76	3.52	2.26
9	10.62	6.43	0.00	9	7.82	3.23	2.06
10	10.31	5.97	0.00	10	6.90	3.13	2.00
11	10.00	5.73	0.00	11	6.21	3.02	1.88
12	9.82	5.39	0.00	12	7.21	2.89	1.72
13	9.06	5.29	0.00	13	7.20	2.95	1.76
14	9.89	5.13	0.00	14	6.81	2.74	1.59

$CO_2 + O_2 + N_2$				$CO_2 + H_2O + O_2 + N_2$			
Cycle No.	CO_2 consumption (mmol.g^{-1})	CO yield (mmol.g^{-1})	H_2 yield (mmol.g^{-1})	Cycle No.	CO_2 consumption (mmol.g^{-1})	CO yield (mmol.g^{-1})	H_2 yield (mmol.g^{-1})
1	9.96	0.00	0.00	1	5.96	0.00	0.00
2	4.34	2.35	0.00	2	5.41	3.94	0.62
3	4.67	2.39	0.00	3	4.56	2.64	0.32
4	4.05	2.08	0.00	4	4.76	1.92	0.08
5	4.30	1.81	0.00	5	4.62	1.44	0.07
6	5.97	1.21	0.00	6	4.15	1.45	0.04
7	4.35	1.22	0.00	7	4.08	1.08	0.05
8	3.93	1.14	0.00	8	4.17	1.02	0.06
9	3.69	1.03	0.00	9	4.06	0.87	0.04
10	3.75	0.88	0.00	10	3.41	0.70	0.02
11	3.73	0.84	0.00	11	3.75	0.74	0.02
12	3.74	0.94	0.00	12	3.32	1.01	0.01
13	3.93	0.85	0.00	13	3.18	0.99	0.02
14	4.00	0.77	0.00	14	2.94	0.89	0.05

in cycle numbers, we still observe a decline in the CO_2 adsorption and conversion performance of DFM. This decrease is likely not associated with carbon deposition, but rather attributable to sintering or other changes within the DFMs. As CO is a toxic and harmful gas, the amount of CO generated during the CO_2 capture stage should be minimised as much as possible.

Figs. 6 and 7, respectively, present the XPS spectra and peak fitting results for the C 1s region of the DFM samples following adsorption under four different flue gas conditions and after 14 cycles. Semi-quantitative analysis was performed on different types of carbon based on the fitting results. The specific Peak Binding Energies (BE) for individual C–C/C=C, C–O, C=O, and O–C=O [65–67] species can be found in Table 1. For the samples that underwent adsorption under ideal conditions, O_2-containing conditions, steam-containing conditions, and simulated flue gas conditions, the atom percentages of C–C/C=C were 53.06%, 43.00%, 43.97%, and 59.27%, respectively. After cyclic processes, these percentages changed to 64.67%, 52.88%, 49.03%, and 39.95%. For the first three conditions, an increase in the percentage of C–C/C=C after cycling indicates the presence of C–C/C=C chemical bonds in the coke. However, under simulated flue gas conditions, the percentage of C–C/C=C decreased after cycling. In contrast, when comparing with the post-adsorption samples, the content of C-O in the cyclic samples increased from 10.78% to 42.45%. This suggests that for the samples that adsorbed under simulated flue gas conditions, the proportion of C-O in coke is higher than C–C/C=C. As for the O–C=O species, it is suggested that the percentage of these species in the cyclic samples is lower than in the post-adsorption samples, implying that O–C=O is the primary form in $CaCO_3$.

3.2. *Product yields and cycle stability in the presence of O_2 and H_2O*

Fig. 8 and Table 2 show the CO_2 consumptions, CO yields and H_2 yields during the CO_2 capture stage under the four different flue gas conditions. As illustrated in Fig. 8 (a), under the ideal condition, the CO yield gradually increased from 4.8 mmol·g^{-1} to 7.8 mmol.g^{-1} between the 2nd and 4th cycles, and subsequently decreased from 7.8 mmol.g^{-1} to 5.8 mmol.g^{-1} from the 5th to the final cycle. The decrease in CO yield can be attributed to the reduced amount of coke due to catalyst performance deterioration as the cycle numbers increase [31,40]. Under the steam-containing condition, the CO yield peaked in the second cycle at 9.9 mmol.g^{-1} but gradually declined in the following cycles, with the CO yield in the final cycle dropping to 3 mmol.g^{-1}. Fig. 8 (b) reveals a decrease in H_2 yield from 5.5 mmol.g^{-1} to 1.5 mmol.g^{-1}. Under the O_2-containing condition, the CO yield was significantly lower, decreasing from 4 mmol.g^{-1} to 1.1 mmol.g^{-1}. As shown in Fig. 8 (b), the H_2 yield under simulated flue gas conditions was much lower, with the highest value in the second cycle at 0.73 mmol.g^{-1}, while the H_2 yield in the subsequent cycles became almost negligible.

As shown in Fig. 8 (c), under the simulated flue gas condition, the CO_2 consumption during the CO_2 capture stage was actually the lowest during the 14 cycles, at 10.7 mmol.g^{-1}. From the 2nd to the 3rd cycle, CO_2 consumption increased to 13.2 mmol.g^{-1}, and then slightly decreased to 10.0 mmol.g^{-1}. The increase in CO_2 consumption from the 2nd cycle onwards is due to the side reaction between CO_2 and coke, while the subsequent decrease should be caused by the reduced CO_2 uptake due to the sintering of CaO [12]. In the presence of steam, the CO_2 consumption in the 1st cycle was 11.5 mmol.g^{-1}, slightly increased to 12.1 mmol.g^{-1} in the 2nd cycle, and gradually decreased to 7.2 mmol.g^{-1} as the number of cycles increased. Since steam can also react with

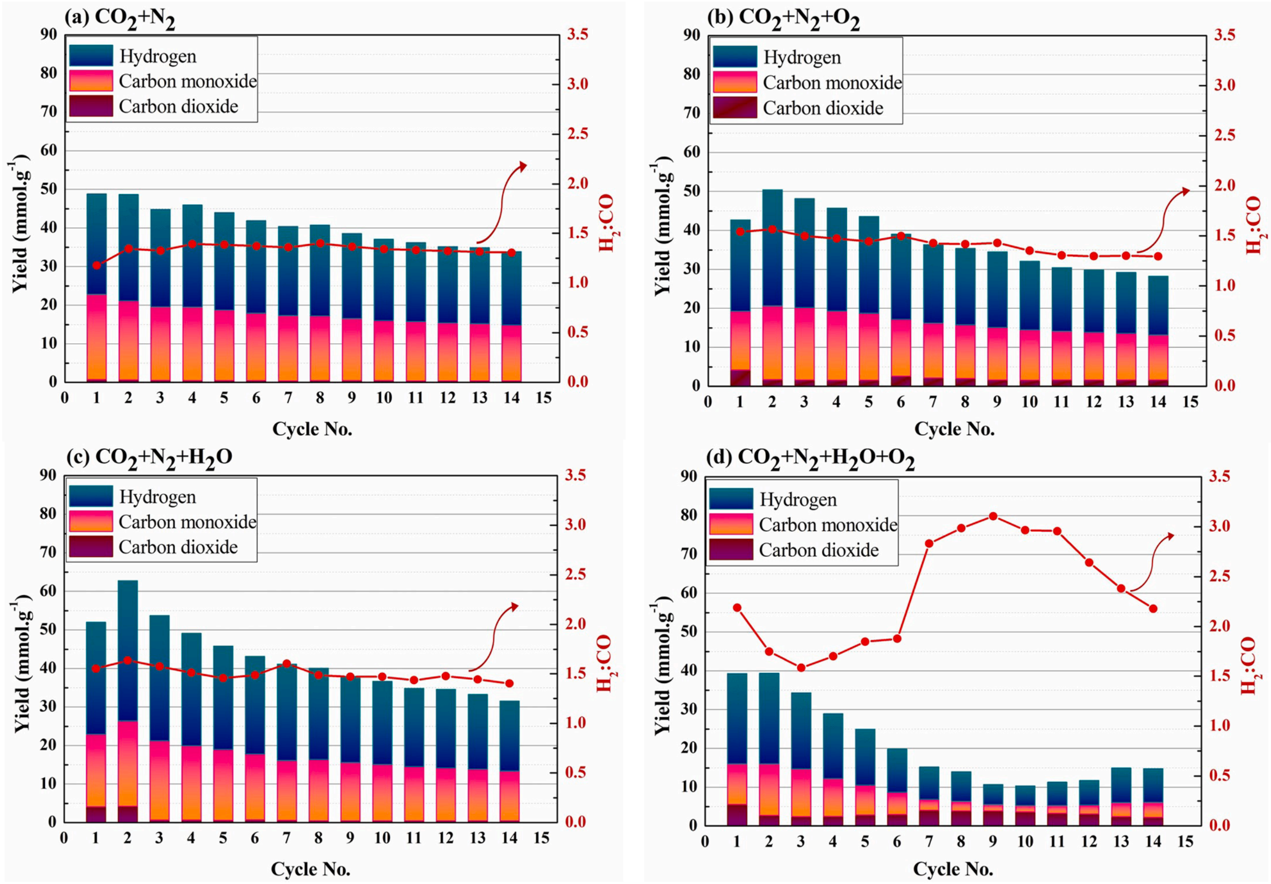

Fig. 9. Yield of CO and H_2 during DRM stage for $Ni_{0.05}/Cao_{0.95}$ under (a) ideal condition (10.0 % CO_2/N_2); (b) O_2-containing condition (10.0 % CO_2 + 6.0 % H_2O/N_2); (c) Steam-containing condition (10.0 % CO_2 + 6.7 % O_2/N_2) and (d) Simulated flue gas condition (10.0 % CO_2 + 6.0 % H_2O + 6.7 % O_2/N_2).

coke and compete with the reaction between CO_2 and coke [68], CO_2 consumption only shows a slight increase. For the O_2-containing condition, the CO_2 consumption in the 1st cycle was 10.0 mmol.g^{-1}, which was similar compared to ideal and steam-containing conditions. As there was no coke formed on the DFM during the 1st cycle, this cycle could reflect the intrinsic CO_2 capacity of the DFM, indicating that O_2 has little effect on the CO_2 capacity of the DFM [69]. In the subsequent cycles, the CO_2 consumption significantly decreased to 4.3 mmol.g^{-1}, due to the additional CO_2 generation by the reaction between O_2 and coke. However, it did not show a further noticeable reduction with increasing cycle numbers, remaining at around 4.3 mmol.g^{-1}. A possible reason for the stability of CO_2 consumption could be that the volume expansion of Ni during the oxidation process acted as a physical barrier to prevent the sintering of CaO [70]. However, under the simulated flue gas conditions, the CO_2 consumption in the first cycle was significantly lower than the other three conditions, only 5.7 mmol.g^{-1}, as shown in Fig. 8 (d). This suggests that the intrinsic CO_2 adsorption performance of the DFM is substantially reduced due to the combined effects of steam and O_2. The CO_2 consumption in the final cycle was only 2.6 mmol.g^{-1}.

The yields of CO, H_2, and CO_2 during the DRM stage are shown in Fig. 9 and Table 3. As depicted in Fig. 9 (a), under the ideal condition, the CO yield gradually decreased from 22.1 mmol.g^{-1} to 14.5 mmol.g^{-1} over 14 cycles, while H_2 decreased from 26.0 mmol.g^{-1} to 18.9 mmol.g^{-1}. The CO_2 yield, however, was almost negligible at less than 0.8 mmol.g^{-1}. As shown in Fig. 9 (b), under the O_2-containing condition, the yields of CO and H_2 were significantly lower compared to the ideal condition, with the highest CO yield being 18.9 mmol.g^{-1} and the lowest 11.6 mmol.g^{-1} during the 14 cycles. Meanwhile, the highest H_2 yield was 29.7 mmol.g^{-1}, and the lowest was 15.1 mmol.g^{-1}. The CO_2 yield was significantly more than the ideal condition, with the highest reaching 4.1 mmol.g^{-1} and the lowest 1.5 mmol.g^{-1}. This suggests that Ni, after being oxidised during the CO_2 capture stage, may not be fully reduced during the DRM stage [36], resulting in lower catalytic performance compared to the ideal condition [40]. Under steam-containing conditions, as shown in Fig. 9 (c) and Table 3, the H_2 yield increased significantly, reaching a maximum of 36.3 mmol.g^{-1} and dropping to 18.1 mmol.g^{-1} after 14 cycles. At the same time, the CO_2 yield also increased, reaching a maximum of 4.3 mmol.g^{-1}, indicating that CH_4 and H_2O underwent the SMR reaction [71] (Eq. (5)). The CO yield was not significantly affected, with the highest being 22.2 mmol.g^{-1} and the lowest 12.9 mmol.g^{-1}. Notably, under the simulated flue gas condition, both CO and H_2 yields were both significantly lower, with the highest CO yield at only 10.6 mmol.g^{-1} and the lowest at 3.9 mmol.g^{-1}. However, the H_2 yield reached 23.2 mmol.g^{-1} during the first two cycles, it was only 8.6 mmol.g^{-1} by the 14th cycle. As shown in Fig. S2, the average yields of CO and H_2 were also the lowest under simulated flue gas conditions. At the same time, the CO_2 yield was obviously higher than the other three conditions, with a maximum of 5.5 mmol.g^{-1} and a minimum of 3.9 mmol.g^{-1}. The lowest CO and H_2 yields among the four conditions suggest that steam can promote the deteriorating effect of O_2 on DFM performance.

3.3. Discussion of the role of steam and O_2 for ICCU-DRM

In this section, we aim to elucidate the impacts of steam and O_2 on the reaction mechanism, focusing primarily on the CO_2 capture stage and the associated changes in the $CaCO_3$ and Ni. The mechanism investigation incorporates a range of characterisation techniques, including in-situ infrared spectroscopy, FIB-SEM, BET surface area analysis, and XPS test.

Table 3
Summary of CO_2, H_2, and CO yields during the DRM stage under ideal condition (10.0 % CO_2/N_2), O_2-containing condition (10.0 % CO_2 + 6.0 % H_2O/N_2), steam-containing condition (10.0 % CO_2 + 6.7 % O_2/N_2) and simulated flue gas condition (10.0 % CO_2 + 6.0 % H_2O + 6.7 % O_2/N_2) of 14 cycles.

$CO_2 + N_2$				$CO_2 + H_2O + N_2$			
Cycle No.	CO_2 yield (mmol.g^{-1})	CO yield (mmol.g^{-1})	H_2 yield (mmol.g^{-1})	Cycle No.	CO_2 yield (mmol.g^{-1})	CO yield (mmol.g^{-1})	H_2 yield (mmol.g^{-1})
1	0.68	22.10	26.04	1	4.12	18.71	29.06
2	0.65	20.47	27.53	2	4.16	22.20	36.33
3	0.55	19.01	25.19	3	0.65	20.58	32.44
4	0.48	19.00	26.48	4	0.58	19.30	29.16
5	0.45	18.22	25.28	5	0.56	18.39	26.81
6	0.41	17.46	23.99	6	0.70	17.01	25.31
7	0.38	16.91	23.02	7	0.50	15.56	24.95
8	0.40	16.79	23.49	8	0.43	15.92	23.68
9	0.40	16.12	22.05	9	0.42	15.18	22.34
10	0.42	15.62	20.99	10	0.45	14.62	21.52
11	0.37	15.35	20.44	11	0.41	14.13	20.28
12	0.35	15.00	19.81	12	0.43	13.73	20.32
13	0.36	14.90	19.62	13	0.43	13.41	19.36
14	0.36	14.51	18.92	14	0.44	12.91	18.14

$CO_2 + O_2 + N_2$				$CO_2 + H_2O + O_2 + N_2$			
Cycle No.	CO_2 yield (mmol.g^{-1})	CO yield (mmol.g^{-1})	H_2 yield (mmol.g^{-1})	Cycle No.	CO_2 yield (mmol.g^{-1})	CO yield (mmol.g^{-1})	H_2 yield (mmol.g^{-1})
1	4.09	15.14	23.34	1	5.45	10.59	23.19
2	1.62	18.94	29.75	2	2.67	13.32	23.28
3	1.53	18.63	27.91	3	2.31	12.36	19.62
4	1.49	17.84	26.34	4	2.39	9.80	16.68
5	1.48	17.19	24.81	5	2.82	7.73	14.28
6	2.53	14.59	21.84	6	2.88	5.85	10.97
7	2.13	14.07	20.06	7	4.01	2.90	8.21
8	1.88	13.82	19.59	8	3.85	2.52	7.52
9	1.58	13.49	19.32	9	3.86	1.65	5.13
10	1.44	13.00	17.57	10	3.53	1.70	5.05
11	1.60	12.50	16.29	11	3.19	2.04	6.03
12	1.59	12.25	15.92	12	3.05	2.36	6.22
13	1.60	11.96	15.56	13	2.32	3.72	8.86
14	1.53	11.62	15.06	14	2.17	3.94	8.58

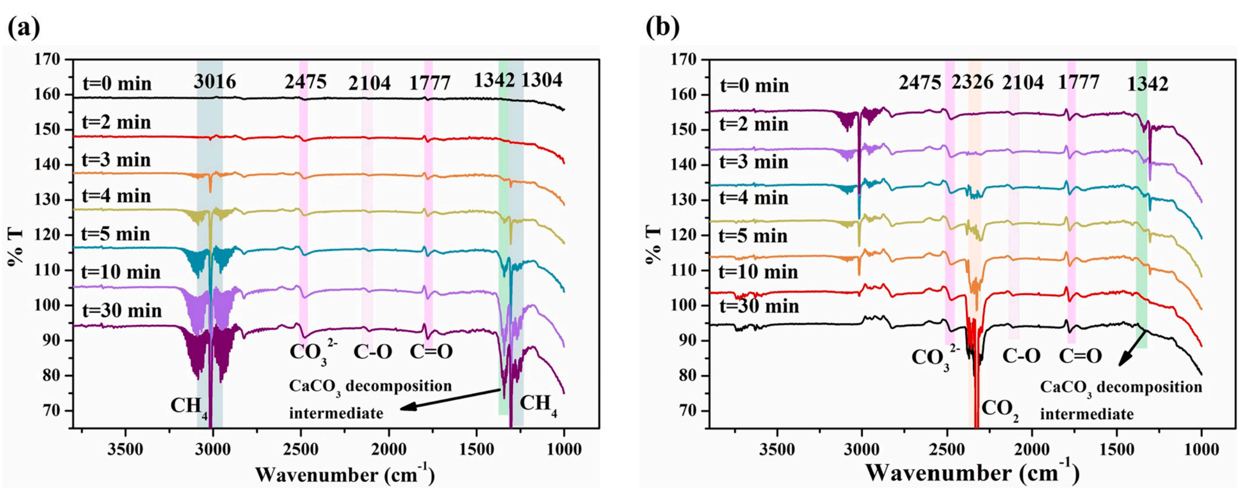

Fig. 10. (a): In-situ Infrared Spectroscopy of $CaCO_3$ decomposition under CH_4; (b): In-situ Infrared Spectroscopy of CO_2 Re-adsorption after $CaCO_3$ Decomposition under CH_4.

Fig. 10 (a) displays the in-situ infrared spectroscopy of $CaCO_3$ decomposition under CH_4, while Fig. 10(b) shows the re-adsorption of CO_2 after this process. As shown in Fig. 10 (a), peaks at 3016 cm^{-1} and 1304 cm^{-1} could be attributed to the C–H vibrations of CH_4 [72]. The 1342 cm^{-1} peak was related to carbonate ions, possibly an intermediate in the $CaCO_3$ and CH_4 reaction [73]. Peaks at 2475 cm^{-1} and 1777 cm^{-1} correspond to CO_3^{2-} [74] and C=O [75,76], while the 2104 cm^{-1} peak was due to C-O bonding[77,78]. It shows that the C=O and carbonate should be the key intermediates of the reaction between CH_4 and $CaCO_3$ during the ICCU-DRM stage. During the re-adsorption of CO_2, as shown in Fig. 10 (b), a split peak at 2326 cm^{-1} resulted from CO_2 gas interference [72]. The 2104 cm^{-1} peak should represent the C-O bond, as it also appeared during the CO_2 capture stage, possibly due to the overlap of CO and C-O in $CaCO_3$. Fig. S3 further support the conclusion, as it demonstrates a stronger 2104 cm^{-1} peak during the DRM stage and a weaker one during CO_2 capture. It is indicated that the decomposition of CO_2 is a critical step in the DRM, further highlighting the vital role of Ni catalysts in the DRM process. This is because Ni provides a surface for reactants to adsorb onto, thereby encouraging collisions between reactants and thus enhancing the reaction rate of the reverse Boudouard

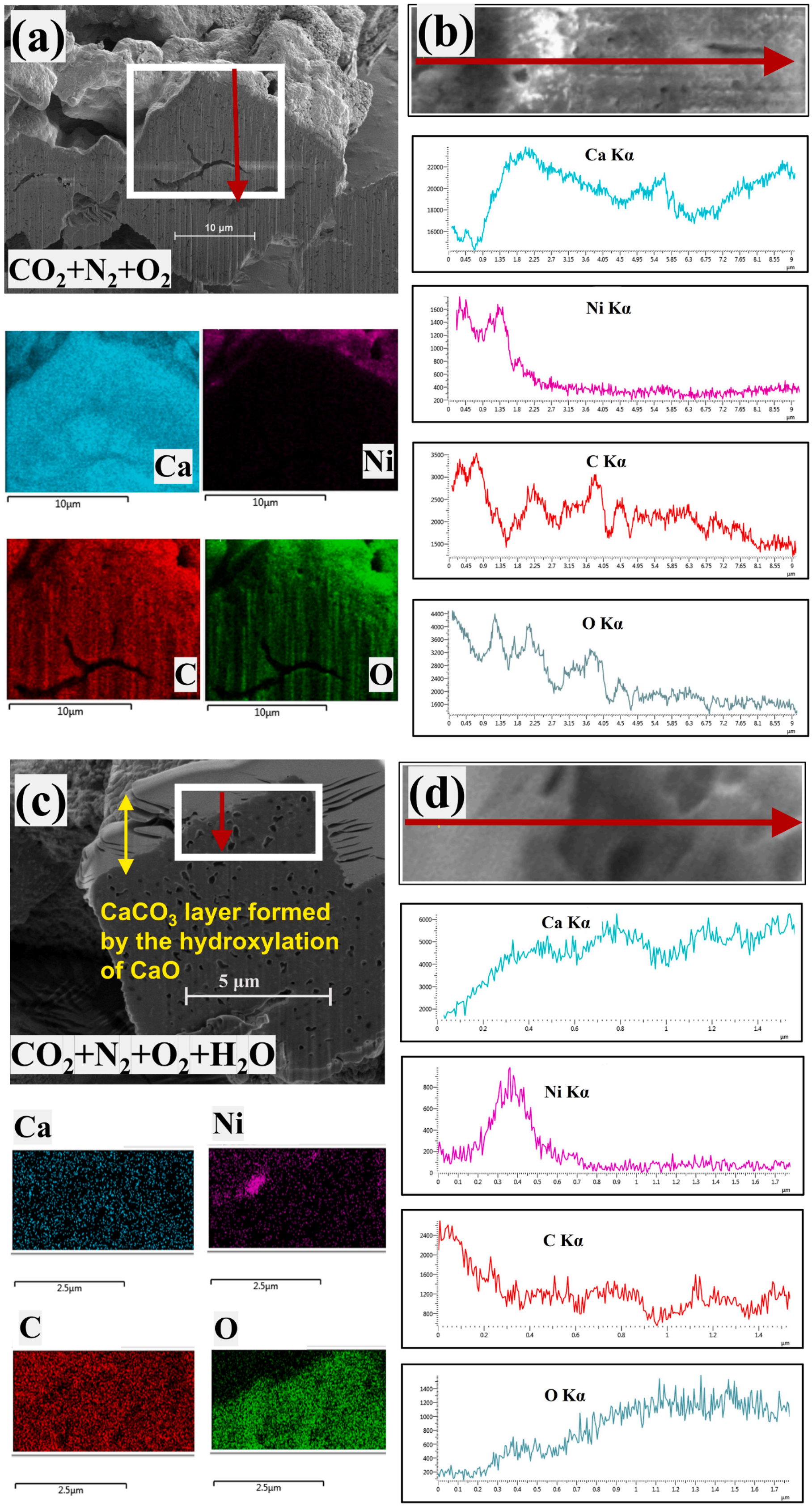

Fig. 11. FIB-SEM/EDX images and EDX elemental mappings of the adsorbed sample under O_2-containing condition (aand b) and under simulated flue gas condition (c and d).

Table 4
Summary of pore size and surface area by BET analysis.

Sample	BET Surface Area ($m^2.g^{-1}$)	Pore volume ($cm^2.g^{-1}$)	Average pore diameter (Å)
A1	1.45	0.00187	57.11
A2	1.04	0.00128	53.92
A3	4.81	0.01341	129.63
A4	0.48	0.00011	14.93

A1: $Ni_{0.05}/CaO_{0.95}$ adsorbed under ideal condition (10% CO_2/N_2).
A2: $Ni_{0.05}/CaO_{0.95}$ adsorbed under O_2-containing condition (10.0 % CO_2 + 6.0 % H_2O/N_2).
A3: $Ni_{0.05}/CaO_{0.95}$ adsorbed under steam-containing condition (10.0 % CO_2 + 6.7 % O_2/N_2).
A4: $Ni_{0.05}/CaO_{0.95}$ adsorbed under simulated flue gas condition (10.0 % CO_2 + 6.0 % H_2O + 6.7 % O_2/N_2).

reaction [79].

The key role of Ni in the catalytic activity of DFMs necessitates a thorough examination of the structural attributes, especially under the influences of steam and O_2, which induce a notable decline in their catalytic efficiency. This reduction can potentially be attributed to the properties of the elemental Ni, requiring further exploration. FIB-SEM was used to probe the cross-sectional morphologies and elemental dissemination within the samples exposed to O_2-containing conditions and simulated flue gas conditions, respectively. In Fig. 11, a comparative analysis of the internal morphological differences of $Ni_{0.05}/Cao_{0.95}$ DFMs subjected to these varying conditions is illustrated. When assessing Fig. 11 (b), a concentration surge of Ni near the surface of samples fully adsorbed under the O_2-containing condition can be observed, with a prominent reduction at approximately 1.4 μm from the surface, denoting a superficial predominance of Ni in the sample. Fig. 11 (a) further elucidates this trend, with EDX mappings of Ni revealing a primary distribution area within the external layer of the sample, while the existence of a void at the center suggests a significantly diminished Ni concentration within the interior of the samples.

On assessing the samples fully adsorbed under simulated flue gas conditions (Fig. 11 (c)), a characteristic of a white outer layer is observed. It is evident that steam significantly influences the morphology of the DFM. As presented in Fig. 11 (d), the examination of Ni elemental concentration reveals a lower concentration in the white area, with the peak value of Ni concentration observed at the intersection of the white outer shell and the interior darker region. This is further corroborated by the EDX mappings of Ni (Fig. 11 (c)), indicating a sparse distribution of Ni throughout the cross-section of the samples. It is suggested that a considerable proportion of Ni is deeply embedded within the sample. Therefore, steam could enhance the dispersion of Ni particles within the samples durin the carbon capture stage.

Table 4 presents the BET test results of the samples subjected to adsorption under four distinct flue gas conditions. The samples fully adsorbed under the steam-containing condition reached the maximum

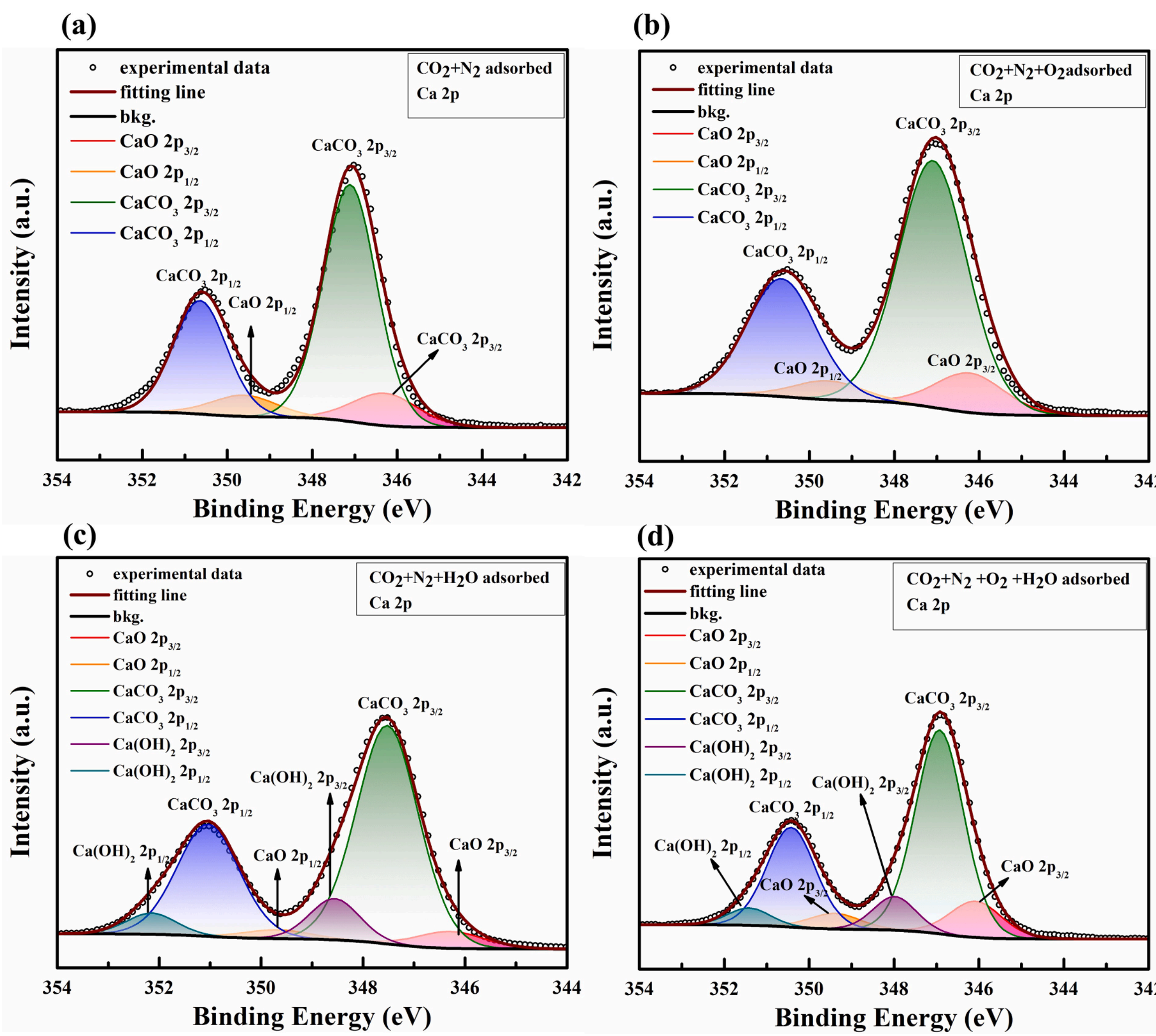

Fig. 12. XPS analysis of Ca 2p region of $Ni_{0.05}/CaO_{0.95}$ after adsorption under (a) ideal condition (10.0 % CO_2/N_2); (b) O_2-containing condition (10.0 % CO_2 + 6.0 % H_2O/N_2); (c) Steam-containing condition (10.0 % CO_2 + 6.7 % O_2/N_2) and (d) Simulated flue gas condition (10.0 % CO_2 + 6.0 % H_2O + 6.7 % O_2/N_2).

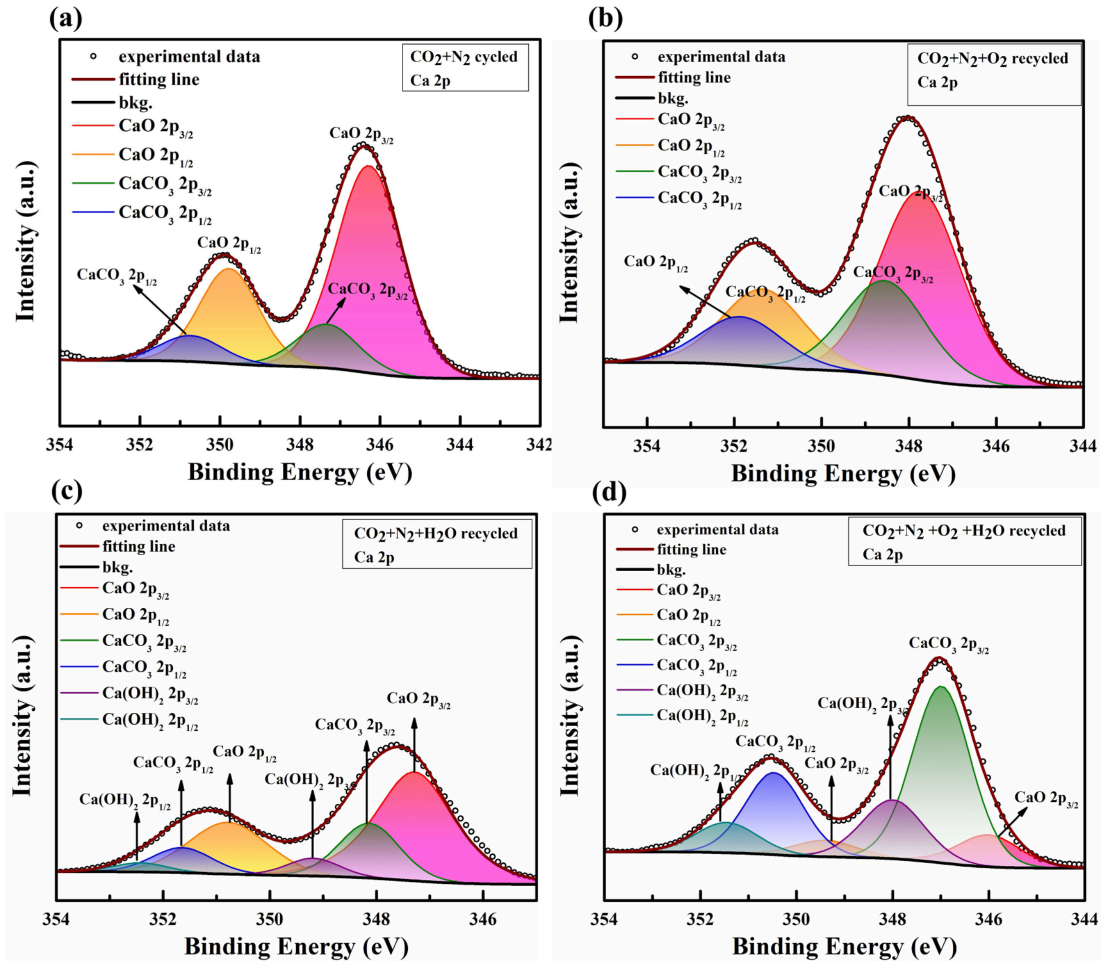

Fig. 13. XPS analysis of Ca 2p region of $Ni_{0.05}/CaO_{0.95}$ after 14 cycles under (a) ideal condition (10.0 % CO_2/N_2); (b) O_2-containing condition (10.0 % CO_2 + 6.0 % H_2O/N_2); (c) Steam-containing condition (10.0 % CO_2 + 6.7 % O_2/N_2) and (d) Simulated flue gas condition (10.0 % CO_2 + 6.0 % H_2O + 6.7 % O_2/N_2).

values of BET surface area, pore volume, and average pore diameter, which were 4.81 $m^2.g^{-1}$, 0.01341 $cm^2.g^{-1}$, and 129.63 Å, respectively. Conversely, under the simulated flue gas condition, these three values were the smallest, specifically 0.48 $m^2.g^{-1}$, 0.00011 $cm^2.g^{-1}$, and 14.93 Å, respectively. The observed decrease in BET surface area, pore volume, and average pore diameter under simulated flue gas conditions implies that the presence of steam and O_2 may negatively impact the structural properties of the samples.

XPS testing for valence states of Ca 2p in the samples offers a novel perspective for elucidating the underlying mechanisms, enhancing the depth and precision of our analysis. Full XPS spectra of adsorbed and cycled samples under different flue gas conditions are shown in Fig. S4. Figs. 12 and 13 illustrate the outcomes of peak fitting for the Ca 2p spectra acquired from XPS analysis of samples following adsorption under four disparate flue gas conditions and samples after 14 reaction cycles, respectively. Fig. S5 displays the semi-quantitative evaluation of the peak fitting, uncovering the atomic percentages of CaO 2p, $CaCO_3$ 2p, and $Ca(OH)_2$ 2p within the Ca 2p elements of each respective sample. The specific Peak Binding Energies (BE) of individual CaO 2p, $CaCO_3$ 2p and $Ca(OH)_2$ 2p [80–82] can be seen in Table 5. Through the comparison of various Ca 2p atom percentages, the adsorption capacity of DFM for CO_2 under diverse flue gas conditions and the regeneration capability of DFM can be assessed.

Taking the samples after adsorption and after cycling under ideal condition as benchmarks, it can be observed that the content of CaO 2p after adsorption is 14.38%, while that of $CaCO_3$ 2p is 85.62%. After cycling, not all $CaCO_3$ can be converted back to CaO; the content of CaO 2p is 83.5%, while that of $CaCO_3$ 2p is 16.5%. In comparison, it can be found that the presence of O_2 alone in the flue gas seems to have little impact on the carbonation of CaO, as CaO 2p is 13.76% and $CaCO_3$ 2p is 86.24%. However, due to the reduction in catalytic performance caused by Ni oxidation, the regeneration capacity of CaO 2p under O_2-containing condition decreases. The content of CaO 2p after cycling is 66.65%, which is lower than that under ideal conditions, and the content of $CaCO_3$ is 16.5%, which is higher than that under ideal condition. Under the steam-containing condition, the content of CaO 2p is significantly reduced compared to the previous two conditions, accounting for only 6.66%, while 81.09% is $CaCO_3$ 2p, and 12.25% is $Ca(OH)_2$ 2p. After cycling, the content of CaO 2p in the sample remains lower than that under the ideal condition, at 68.4%, with $CaCO_3$ 2p content at 24.64%, and 6.96% of $Ca(OH)_2$ 2p. This indicates that although previous studies have suggested that steam is favorable for CO_2 adsorption, the increased thickness of the formed $CaCO_3$ [83] layer could encapsulate the catalyst, thereby reducing catalytic performance and hindering the decomposition of $CaCO_3$ and the regeneration of CaO.

For the sample adsorbed under simulated flue gas conditions, the content of CaO 2p is 14.07%, that of $CaCO_3$ 2p is 74.97%, and $Ca(OH)_2$ 2p accounts for 10.96%. Upon comparison with the sample after adsorption under water-containing conditions, a decline in the contents of $CaCO_3$ 2p and $Ca(OH)_2$ 2p is evident. In conjunction with the prior analysis, this phenomenon may be attributed to the rapid oxidation of Ni and the formation of a $CaCO_3$ layer on the surface. Such processes obstruct the penetration of steam and CO_2 into the sample interior, consequently causing a certain level of blockage on the surface and

Table 5
Summary of atomic ratio of Ca 2p by XPS analysis.

Sample	Name	Peak BE	Atomic %
A1	CaO $2p_{3/2}$	346.29	14.38
	CaO $2p_{1/2}$	349.61	
	$CaCO_3$ $2p_{3/2}$	347.11	85.62
	$CaCO_3$ $2p_{3/2}$	350.64	
A2	CaO $2p_{3/2}$	346.23	13.76
	CaO $2p_{1/2}$	349.57	
	$CaCO_3$ $2p_{3/2}$	347.09	86.24
	$CaCO_3$ $2p_{1/2}$	350.66	
A3	CaO $2p_{3/2}$	346.28	6.66
	CaO $2p_{1/2}$	349.69	
	$CaCO_3$ $2p_{3/2}$	347.52	81.09
	$CaCO_3$ $2p_{1/2}$	351.04	
	$Ca(OH)_2$ $2p_{3/2}$	348.56	12.25
	$Ca(OH)_2$ $2p_{1/2}$	352.15	
A4	CaO $2p_{3/2}$	346.08	14.07
	CaO $2p_{1/2}$	349.4	
	$CaCO_3$ $2p_{3/2}$	346.93	74.97
	$CaCO_3$ $2p_{3/2}$	350.42	
	$Ca(OH)_2$ $2p_{3/2}$	347.99	10.96
	$Ca(OH)_2$ $2p_{1/2}$	351.42	
C1	CaO $2p_{3/2}$	346.27	83.50
	CaO $2p_{1/2}$	349.77	
	$CaCO_3$ $2p_{3/2}$	347.32	16.50
	$CaCO_3$ $2p_{3/2}$	350.73	
C2	CaO $2p_{3/2}$	347.74	66.65
	CaO $2p_{1/2}$	351.34	
	$CaCO_3$ $2p_{3/2}$	348.54	33.35
	$CaCO_3$ $2p_{1/2}$	351.84	
C3	CaO $2p_{3/2}$	347.29	68.40
	CaO $2p_{1/2}$	350.78	
	$CaCO_3$ $2p_{3/2}$	348.13	24.64
	$CaCO_3$ $2p_{1/2}$	351.64	
	$Ca(OH)_2$ $2p_{3/2}$	349.18	6.96
	$Ca(OH)_2$ $2p_{1/2}$	352.42	
C4	CaO $2p_{3/2}$	346.01	12.43
	CaO $2p_{1/2}$	349.41	
	$CaCO_3$ $2p_{3/2}$	346.99	64.67
	$CaCO_3$ $2p_{3/2}$	350.46	
	$Ca(OH)_2$ $2p_{3/2}$	348.00	22.90
	$Ca(OH)_2$ $2p_{1/2}$	351.45	

A1: $Ni_{0.05}/CaO_{0.95}$ adsorbed under ideal condition (10% CO_2/N_2).
A2: $Ni_{0.05}/CaO_{0.95}$ adsorbed under O_2-containing condition (10.0 % CO_2 + 6.0 % H_2O/N_2).
A3: $Ni_{0.05}/CaO_{0.95}$ adsorbed under steam-containing condition (10.0 % CO_2 + 6.7 % O_2/N_2).
A4: $Ni_{0.05}/CaO_{0.95}$ adsorbed under simulated flue gas condition (10.0 % CO_2 + 6.0 % H_2O + 6.7 % O_2/N_2).
C1: $Ni_{0.05}/CaO_{0.95}$ regenerated after 14 cycles under ideal condition.
C2: $Ni_{0.05}/CaO_{0.95}$ regenerated after 14 cycles under O_2-containing condition.
C3: $Ni_{0.05}/CaO_{0.95}$ regenerated after 14 cycles under steam-containing condition.
C4: $Ni_{0.05}/CaO_{0.95}$ regenerated after 14 cycles under simulated flue gas condition.

leading to a reduction in the amount of CaO subjected to carbonation and hydroxylation. The most crucial information pertains to the sample after cycling, in which the contents of CaO 2p, $CaCO_3$ 2p, and $Ca(OH)_2$ 2p are 12.43 %, 64.67 %, and 22.9 %, respectively. The sample appears nearly unchanged compared to its state after adsorption. This suggests that under simulated flue gas conditions, the capability of DFM regeneration is poor.

Based on the characterisation results of in-situ infrared, FIB-SEM, BET surface area analysis, and XPS analysis, we have analysed the influence mechanism of steam and O_2 on DMF. Through the characterisation results of in-situ infrared and the analysis of the cause of the pre-reaction duration mentioned earlier, it is confirmed that Ni in the non-oxidised state plays a critical role in the progress of DRM. In other words, Ni in the oxidised state exhibits almost no catalytic activity and needs to be reduced by CH_4 first to initiate DRM. It is suggested that after the reduction of NiO in DMF, $CaCO_3$ could be decomposed to generate CO_2, reacting with CH_4. Therefore, the internal structural differences of DMF after adsorption were compared under O_2-containing conditions and simulated flue gas conditions using FIB-SEM. As the presence of steam accelerated the expansion of CaO [57,84–86], thereby encapsulating NiO (Fig. S6). Therefore, the NiO in DMF after adsorption under simulated flue gas conditions is more difficult to reduce compared to that under O_2-containing conditions.

It was found that under simulated flue gas conditions, the DMF samples post-adsorption exhibited the lowest values for BET surface area, pore volume, and average pore diameter. This trend was not replicated in the samples adsorbed under steam-containing conditions. Based on these observations, it can be recognised as a connection to the specific oxidative processes of Ni. Due to the volumetric expansion that Ni [21,51,87] undergoes during the oxidation process, which is also a feature of CaO absorption of CO_2, the simultaneous action of both elements results in a swift formation of a dense shell on the surface of the DFM. This is particularly the case when steam is present, as it accelerates the absorption of CO_2 and promotes this expansion. This phenomenon can be confirmed by the outer white section of the sample in Fig. 11 (c).

This shell formation leads to a decrease in the permeability of CH_4 into the sample, inhibiting its contact with NiO for the reduction process. Therefore, a significant portion of NiO was permanently embedded within the DFM, reducing its reducibility and causing a loss in catalytic activity. In the absence of Ni, it becomes difficult for $CaCO_3$ to decompose quickly. Therefore, the regenerative capability of DFMs under simulated flue gas conditions is significantly reduced, as revealed by the XPS testing results and leads to a significant decrease in the yields of CO and H_2 (Fig. 9).

4. Conclusions

In conclusion, this study systematically investigated the ICCU-DRM process under various flue gas conditions, focusing on the effects of O_2 and steam. These results offer valuable insights into the effects of O_2 and steam on the ICCU-DRM process and emphasise the need to consider these factors in the design and operation of practical industrial applications. The key findings are as follows:

(1) O_2 alone in the flue gas (10.0 % CO_2 + 6.7 % O_2/N_2) negatively affects the DRM performance of the DFM, reducing the highest CO yield and H_2 from 22.1 mmol.g^{-1} to 18.9 mmol.g^{-1} and from 18.9 mmol.g^{-1} to 15.1 mmol.g^{-1} compared to the ideal condition (10% CO_2/N_2), respectively, primarily due to the generation of extra CO_2 from O_2 reacting with coke and oxidising Ni.
(2) FIB-SEM/EDX images and EDX elemental mappings show that the presence of steam in the flue gas (10.0 % CO_2 + 6.0 % H_2O + 6.7 % O_2/N_2) results in NiO encapsulation by $CaCO_3$, which hinders NiO reduction by CH_4 and leads to a decrease in catalytic performance with lowest CO yield of 3.9 mmol.g^{-1} and H_2 yield of only 8.6 mmol.g^{-1}.
(3) The formation of a $CaCO_3$ shell layer due to rapid CO_2 adsorption under simulated flue gas conditions is the primary reason for the reduction in surface area and pore size, with surface area, pore volume, and average pore diameter of 0.48 m^2.g^{-1}, 0.00011 cm^2.g^{-1}, and 14.93 Å, respectively. XPS analysis confirms these findings, revealing that the presence of both O_2 and steam in the flue gas significantly reduces the regenerative capability of DFM.

As after adsorption, the content of CaO 2p was 14.07%, $CaCO_3$ 2p was 74.97%, and $Ca(OH)_2$ 2p was 10.96%. After 14 cycles the contents of CaO 2p, $CaCO_3$ 2p, and $Ca(OH)_2$ 2p were 12.43 %, 64.67 %, and 22.9 %, nearly unchanged compared to the samples after adsorption.

With the current understanding of the interaction mechanism between steam and O_2, there is a compelling need for the development of innovative strategies to prevent or mitigate the effect of their simultaneous presence. This has become more feasible and urgently necessary, given their observed impact on the ICCU-DRM process. Effective strategies might involve refining the structure of catalysts, particularly adjusting how catalysts are distributed on sorbents. The goal of these adjustments is to ensure the catalysts are positioned in a way that prevents them from being encapsulated by $CaCO_3$ after the CO_2 capture stage. It is vital to guarantee that the catalyst is reduced during the DRM stage, thereby ensuring the restoration of its catalytic performance. Moreover, system-level improvements could also be introduced to address this issue. For instance, incorporating metal elements at the front end of DFM could serve to reduce the O_2 content, while the addition of desiccants could minimise the level of steam, thereby diminishing the possibility of simultaneous existence of O_2 and steam. This approach presents another possible innovation for optimising the ICCU-DRM process. Through the implementation of these two measures, the practical applicability of the process in industrial scenarios could be enhanced, potentially leading to improved performance and increased system stability.

CRediT authorship contribution statement

Xiaotong Zhao: Investigation, Formal analysis, Data curation, Methodology, Writing - original draft. **Shuzhuang Sun:** Methodology, Formal analysis, Investigation. **Yingrui Zhang:** Investigation, Formal analysis. **Yuanyuan Wang:** Investigation, Formal analysis. **Yuan Zhu:** Investigation, Formal analysis. **Paul Williams:** FIB-SEM test, Review & editing. **Shaoliang Guan:** Investigation. **Chunfei Wu:** Conceptualization, Writing – review & editing, Supervision, Project administration, Funding acquisition.

Declaration of Competing Interest

The authors declare that they have no known competing financial interests or personal relationships that could have appeared to influence the work reported in this paper.

Data availability

The authors are unable or have chosen not to specify which data has been used.

Acknowledgements

This project has received funding from the European Union's Horizon 2020 research and innovation programme under the Marie Skłodowska-Curie grant agreement No 823745. We also acknowledge for the XPS data collection performed at the EPSRC National Facility for XPS ('HarwellXPS'), operated by Cardiff University and UCL, under contract No. PR16195.

Appendix A. Supplementary material

Supplementary data to this article can be found online at https://doi.org/10.1016/j.seppur.2023.124866.

References

[1] F. Song, G.J. Zhang, V. Ramanathan, L.R. Leung, Trends in surface equivalent potential temperature: a more comprehensive metric for global warming and weather extremes, Proc. Natl. Acad. Sci. 119 (2022) e2117832119.
[2] E.I. Koytsoumpa, D. Magiri – Skouloudi, S. Karellas, E. Kakaras, Bioenergy with carbon capture and utilisation: A review on the potential deployment towards a European circular bioeconomy, Renew. Sust. Energy Rev. 152 (2021) 111641.
[3] Z. Hao, M.H. Barecka, A.A.J.E. Lapkin, E. Science, Accelerating net zero from the perspective of optimising a carbon capture and utilisation system 15 (2022) 2139–2153.
[4] J.C.M. Pires, F.G. Martins, M.C.M. Alvim-Ferraz, M. Simões, Recent developments on carbon capture and storage: an overview, Chem. Eng. Res. Des. 89 (2011) 1446–1460.
[5] Y. Wang, Z. Pan, W. Zhang, T.N. Borhani, R. Li, Z. Zhang, Life cycle assessment of combustion-based electricity generation technologies integrated with carbon capture and storage: a review, Environ. Res. 207 (2022), 112219.
[6] A. Babin, C. Vaneeckhaute, M.C. Iliuta, Potential and challenges of bioenergy with carbon capture and storage as a carbon-negative energy source: a review, Biomass Bioenergy 146 (2021), 105968.
[7] Y. Qiao, C. Wu, Nitrogen enriched biochar used as CO_2 adsorbents: a brief review, Carbon Capt. Sci. Technol. 2 (2022).
[8] M.A. Sabri, S. Al Jitan, D. Bahamon, L.F. Vega, G. Palmisano, Current and future perspectives on catalytic-based integrated carbon capture and utilisation, Sci. Total Environ. 790 (2021), 148081.
[9] S. Sun, Y. Wang, X. Zhao, C. Zhang, C. Wu, One step upcycling CO_2 from flue gas into CO using natural stone in an integrated CO_2 capture and utilisation system, Carbon Capt. Sci. Technol. 5 (2022), 100078.
[10] S. Sun, H. Sun, P.T. Williams, C. Wu, Recent advances in integrated CO_2 capture and utilisation: a review, Sust. Energy Fuel 5 (2021) 4546–4559.
[11] S. Masoudi Soltani, A. Lahiri, H. Bahzad, P. Clough, M. Gorbounov, Y. Yan, Sorption-enhanced steam methane reforming for combined co_2 capture and hydrogen production: a state-of-the-art review, Carbon Capt. Sci. Technol. 1 (2021), 100003.
[12] M. Krodel, A. Landuyt, P.M. Abdala, C.R. Muller, Mechanistic understanding of CaO-based sorbents for high-temperature CO_2 capture: advanced characterisation and prospects, ChemSusChem 13 (2020) 6259–6272.
[13] X. Ma, X. Li, H. Cui, W. Zhang, Z. Cheng, Z. Zhou, Metal oxide-doped Ni/CaO dual-function materials for integrated CO_2 capture and conversion: performance and mechanism, AIChE J 69 (2021) e17520.
[14] S. Sun, C. Zhang, S. Chen, X. Zhao, Y. Wang, S. Xu, C. Wu, Integrated CO_2 capture and reverse water-gas shift reaction over CeO_2-CaO dual functional materials, R Soc Open Sci 10 (2023), 230067.
[15] J. Hu, P. Hongmanorom, P. Chirawatkul, S. Kawi, Efficient integration of CO_2 capture and conversion over a Ni supported CeO_2-modified CaO microsphere at moderate temperature, Chem. Eng. J. 426 (2021) 13.
[16] S. Jo, H.D. Son, T.-Y. Kim, J.H. Woo, D.Y. Ryu, J.C. Kim, S.C. Lee, K.L. Gilliard-AbdulAziz, Ru/K_2CO_3–MgO catalytic sorbent for integrated CO_2 capture and methanation at low temperatures, Chem. Eng. J. 469 (2023), 143772.
[17] B. Jin, T. Ouyang, Z. Zhang, Y. Zhao, H. Zhang, W. Yao, G. Huang, Z. Liang, Prussian blue derived Ca-Fe bifunctional materials for chemical looping CO_2 capture and in-situ conversion, Sep. Purif. Technol. 123975 (2023).
[18] N. Wang, Y. Feng, L. Liu, X. Guo, Effects of preparation methods on the structure and property of Al-stabilized CaO-based sorbents for CO_2 capture, Fuel Process. Technol. 173 (2018) 276–284.
[19] J. Wu, Y. Zheng, J. Fu, Y. Guo, J. Yu, J. Chu, P. Huang, C. Zhao, Synthetic Ni–CaO–CeO_2 dual function materials for integrated CO_2 capture and conversion via reverse water–gas shift reaction, Sep. Purif. Technol. 317 (2023).
[20] P. Jamrunroj, S. Wongsakulphasatch, A. Maneedaeng, C.K. Cheng, S. Assabumrungrat, Surfactant assisted CaO-based sorbent synthesis and their application to high-temperature CO_2 capture, Powder Technol. 344 (2019) 208–221.
[21] P. Xu, M. Xie, Z. Cheng, Z. Zhou, CO_2 capture performance of CaO-based sorbents prepared by a sol-gel method, Ind. Eng. Chem. Res. 52 (2013) 12161–12169.
[22] L.-P. Merkouri, J.L. Martín-Espejo, L.F. Bobadilla, J.A. Odriozola, A. Penkova, T. Ramirez Reina, M.S. Duyar, Unravelling the CO_2 capture and conversion mechanism of a NiRu–Na_2O switchable dual-function material in various CO_2 utilisation reactions, J. Mater. Chem. A 11 (2023) 13209–13216.
[23] Y. Guo, G. Wang, J. Yu, P. Huang, J. Sun, R. Wang, T. Wang, C. Zhao, Tailoring the performance of Ni-CaO dual function materials for integrated CO_2 capture and conversion by doping transition metal oxides, Sep. Purif. Technol. 305 (2023).
[24] Y.-N. Li, L.-N. He, A.-H. Liu, X.-D. Lang, Z.-Z. Yang, B. Yu, C.-R. Luan, In situ hydrogenation of captured CO_2 to formate with polyethyleneimine and Rh/monophosphine system, Green Chem. 15 (2013) 2825.
[25] S. Kameoka, K. Kita, T. Takeda, S. Tanaka, S. Ito, K. Yuzaki, T. Miyadera, K. Kunimori, Simultaneous removal of N_2O and CH_4 as the strong greenhouse-effect gases over Fe-BEA zeolite in the presence of excess O_2, Catal. Lett. 69 (2000) 169–173.
[26] W.-J. Jang, J.-O. Shim, H.-M. Kim, S.-Y. Yoo, H.-S. Roh, A review on dry reforming of methane in aspect of catalytic properties, Catal. Today 324 (2019) 15–26.
[27] N.V. Ruban, V.N. Rogozhnikov, O.A. Stonkus, V.A. Emelyanov, V.P. Pakharukova, D.A. Svintsitskiy, S.V. Zazhigalov, A.N. Zagoruiko, P.V. Snytnikov, V.A. Sobyanin, D.I. Potemkin, A comparative investigation of equimolar Ni-, Ru-, Rh- and Pt-based composite structured catalysts for energy-efficient methane reforming, Fuel 352 (2023).

[28] Y. Mao, L. Zhang, X. Zheng, W. Liu, Z. Cao, H. Peng, Coke-resistance over Rh–Ni bimetallic catalyst for low temperature dry reforming of methane, Int. J. Hydrogen Energy 48 (2023) 13890–13901.
[29] Z. Liu, F. Zhang, N. Rui, X. Li, L. Lin, L.E. Betancourt, D. Su, W. Xu, J. Cen, K. Attenkofer, H. Idriss, J.A. Rodriguez, S.D. Senanayake, Highly active ceria-supported Ru catalyst for the dry reforming of methane: in situ identification of $Ru^{\delta+}$–Ce^{3+} interactions for enhanced conversion, ACS Catal. 9 (2019) 3349-3359.
[30] R. Zhou, Y. Ren, Q. Lu, N. Mahinpey, Microwave-assisted hydrothermal synthesis of Ru/CeO_2 catalyst for efficient and stable low-temperature dry reforming of methane, Fuel 346 (2023).
[31] D. Wang, P. Littlewood, T.J. Marks, P.C. Stair, E. Weitz, Coking can enhance product yields in the dry reforming of methane, ACS Catal. 12 (2022) 8352–8362.
[32] S. Jo, J.H. Lee, J.H. Woo, T.-Y. Kim, H.-J. Ryu, B. Hwang, J.C. Kim, S.C. Lee, K. L. Gilliard-AbdulAziz, Coke-promoted Ni/CaO catal-sorbents in the production of cyclic CO and syngas, Sust. Energy Fuel 6 (2022) 81–88.
[33] S.M. Kim, P.M. Abdala, M. Broda, D. Hosseini, C. Copéret, C. Müller, Integrated CO_2 capture and conversion as an efficient process for fuels from greenhouse gases, ACS Catal. 8 (2018) 2815–2823.
[34] X. Zhang, Y. Xu, G. Zhang, C. Wu, J. Liu, Y. Lv, Nitrogen-doped porous carbons derived from sustainable biomass via a facile post-treatment nitrogen doping strategy: efficient CO_2 capture and DRM, Int. J. Hydrogen Energy 47 (2022) 24388–24397.
[35] B. Shao, Z.Q. Wang, X.Q. Gong, H. Liu, F. Qian, P. Hu, J. Hu, Synergistic promotions between CO_2 capture and in-situ conversion on Ni-CaO composite catalyst, Nat Commun 14 (2023) 996.
[36] A. Bermejo-López, B. Pereda-Ayo, J.A. Onrubia-Calvo, J.A. González-Marcos, J. R. González-Velasco, How the presence of O_2 and NOx influences the alternate cycles of CO_2 adsorption and hydrogenation to CH_4 on Ru-Na-Ca/Al_2O_3 dual function material, J. CO_2 Util. 67 (2023), 102343.
[37] S. Champagne, D.Y. Lu, A. Macchi, R.T. Symonds, E.J. Anthony, Influence of steam injection during calcination on the reactivity of cao-based sorbent for carbon capture, Ind. Eng. Chem. Res. 52 (2013) 2241–2246.
[38] G. Angajala, S.J.I. Radhakrishnan, C. Signaling, A review on nickel nanoparticles as effective therapeutic agents for inflammation, Inflam. Cell Signal. 1 (2014) 1–8.
[39] T.A. Le, Q.C. Do, Y. Kim, T.-W. Kim, H.-J. Chae, A review on the recent developments of ruthenium and nickel catalysts for CO_x-free H_2 generation by ammonia decomposition, Korean J. Chem. Eng. 38 (2021) 1087–1103.
[40] S. Sun, Y. Zhang, C. Li, Y. Wang, C. Zhang, X. Zhao, H. Sun, C. Wu, Upgrading CO_2 from simulated power plant flue gas via integrated CO_2 capture and dry reforming of methane using Ni-CaO, Sep. Purif. Technol. 308 (2023), 122956.
[41] S.A. Mazari, N. Hossain, W.J. Basirun, N.M. Mubarak, R. Abro, N. Sabzoi, A. Shah, An overview of catalytic conversion of CO_2 into fuels and chemicals using metal organic frameworks, Process Saf. Environ. Prot. 149 (2021) 67–92.
[42] G. Centi, S. Perathoner, G. Papanikolaou, Plasma assisted CO_2 splitting to carbon and oxygen: a concept review analysis, Journal of CO_2 Utilization 54 (2021), 101775.
[43] P.K. Chaudhary, N. Koshta, G. Deo, Effect of O_2 and temperature on the catalytic performance of Ni/Al_2O_3 and Ni/$MgAl_2O_4$ for the dry reforming of methane (DRM), Int. J. Hydrogen Energy 45 (2020) 4490–4500.
[44] C.A. Querini, S.C. Fung, Temperature-programmed oxidation technique: kinetics of coke-O_2 reaction on supported metal catalysts, Appl. Catal. A 117 (1994) 53–74.
[45] S. He, S. Li, L. Gao, Proposal and energy saving analysis of novel methanol–electricity polygeneration system based on staged coal gasification method, Energ. Conver. Manage. 233 (2021).
[46] E. Pawelczyk, I. Wysocka, J. Gębicki, Pyrolysis combined with the dry reforming of waste plastics as a potential method for resource recovery—a review of process parameters and catalysts, Catalysts 12 (2022) 362–391.
[47] A. Abdulrasheed, A.A. Jalil, Y. Gambo, M. Ibrahim, H.U. Hambali, M.Y. Shahul Hamid, A review on catalyst development for dry reforming of methane to syngas: recent advances, Renew. Sustain. Energy Rev. 108 (2019) 175–193.
[48] P. Boldrin, E. Ruiz-Trejo, J. Mermelstein, J.M. Bermúdez Menéndez, T. Ramírez Reina, N.P. Brandon, Strategies for Carbon and Sulfur Tolerant Solid Oxide Fuel Cell Materials, Incorporating Lessons from Heterogeneous Catalysis, Chem. Rev. 116 (2016) 13633-13684.
[49] H. Seo, Recent scientific progress on developing supported Ni catalysts for Dry (CO_2) reforming of methane, Catalysts 8 (2018) 110–128.
[50] N.A.K. Aramouni, J.G. Touma, B.A. Tarboush, J. Zeaiter, M.N. Ahmad, Catalyst design for dry reforming of methane: analysis review, Renew. Sustain. Energy Rev. 82 (2018) 2570–2585.
[51] S. Sun, C. Zhang, S. Guan, S. Xu, P.T. Williams, C. Wu, Ni/support-CaO bifunctional combined materials for integrated CO_2 capture and reverse water-gas shift reaction: influence of different supports, Sep. Purif. Technol. 298 (2022), 121604.
[52] Z. Rao, Y. Cao, Z. Huang, Z. Yin, W. Wan, M. Ma, Y. Wu, J. Wang, G. Yang, Y. Cui, Z. Gong, Y. Zhou, Insights into the nonthermal effects of light in dry reforming of methane to enhance the H_2/CO ratio near unity over Ni/Ga_2O_3, ACS Catal. 11 (2021) 4730–4738.
[53] J. Niu, F. Guo, J. Ran, W. Qi, Z. Yang, Methane dry (CO_2) reforming to syngas (H_2/CO) in catalytic process: from experimental study and DFT calculations, Int. J. Hydrogen Energy 45 (2020) 30267–30287.
[54] H.J. Gallon, X. Tu, M.V. Twigg, J.C. Whitehead, Plasma-assisted methane reduction of a NiO catalyst—low temperature activation of methane and formation of carbon nanofibres, Appl. Catal. B 106 (2011) 616–620.
[55] R. Pereñiguez, V.M. Gonzalez-delaCruz, A. Caballero, J.P. Holgado, $LaNiO_3$ as a precursor of Ni/La_2O_3 for CO_2 reforming of CH_4: effect of the presence of an amorphous NiO phase, Appl. Catal. B 123–124 (2012) 324–332.
[56] L. Barelli, G. Bidini, F. Gallorini, S. Servili, Hydrogen production through sorption-enhanced steam methane reforming and membrane technology: a review, Energy 33 (2008) 554–570.
[57] N. Wang, Y. Feng, X. Guo, A.C.T. van Duin, Insights into the role of H_2O in the carbonation of CaO nanoparticle with CO_2, J. Phys. Chem. C 122 (2018) 21401–21410.
[58] G. Montes-Hernandez, R. Chiriac, F. Toche, F. Renard, Gas–solid carbonation of $Ca(OH)_2$ and CaO particles under non-isothermal and isothermal conditions by using a thermogravimetric analyser: implications for CO_2 capture, Int. J. Greenhouse Gas Control 11 (2012) 172–180.
[59] E. le Saché, T.R. Reina, Analysis of Dry Reforming as direct route for gas phase CO_2 conversion. The past, the present and future of catalytic DRM technologies, Prog. Energy Combust. Sci. 89 (2022), 100970.
[60] K. Sato, R. Saito, Y. Oyama, J. Jiang, L.G. Cançado, M.A. Pimenta, A. Jorio, G. G. Samsonidze, G. Dresselhaus, M.S. Dresselhaus, D-band Raman intensity of graphitic materials as a function of laser energy and crystallite size, Chem. Phys. Lett. 427 (2006) 117–121.
[61] A. Jorio, A.G. Souza Filho, G. Dresselhaus, M.S. Dresselhaus, A.K. Swan, M.S. Ünlü, B.B. Goldberg, M.A. Pimenta, J.H. Hafner, C.M. Lieber, R. Saito, G-band resonant Raman study of 62 isolated single-wall carbon nanotubes, Phys. Rev. B 65 (2002), 155412.
[62] J.S. Park, A. Reina, R. Saito, J. Kong, G. Dresselhaus, M.S. Dresselhaus, G′ band Raman spectra of single, double and triple layer graphene, Carbon 47 (2009) 1303–1310.
[63] T.N. Zavaritskaya, N.N. Melnik, F.A. Pudonin, I.A. Sherstnev, Multilayer graphene structure of carbon in short-period superlattices, JETP Lett. 103 (2016) 341–344.
[64] O.A. Maslova, M.R. Ammar, G. Guimbretière, J.N. Rouzaud, P. Simon, Determination of crystallite size in polished graphitised carbon by Raman spectroscopy, Phys. Rev. B 86 (2012), 134205.
[65] G. Beamson, D. Clark, N. Hayes, D. Law, Observation of electrical conductivity during XPS analysis of organic oils, Surf. Sci. Spectra 3 (1994) 366–374.
[66] W.J. Landis, J.R. Martin, X-ray photoelectron spectroscopy applied to gold-decorated mineral standards of biological interest, J. Vac. Sci. Technol. A 2 (1984) 1108–1111.
[67] K.L. Smith, K.M. Black, Characterization of the treated surfaces of silicon alloyed pyrolytic carbon and SiC, J. Vac. Sci. Technol. A 2 (1984) 744–747.
[68] F. Tang, Y. Chi, Y. Jin, Z. Zhu, J. Ma, Gasification characteristics of a simulated waste under separate and mixed atmospheres of steam and CO_2, Fuel 317 (2022).
[69] A.P. Hallenbeck, J.R. Kitchin, Effects of O_2 and SO_2 on the capture capacity of a primary-amine based polymeric CO_2 sorbent, Ind. Eng. Chem. Res. 52 (2013) 10788–10794.
[70] M. Shokrollahi Yancheshmeh, H.R. Radfarnia, M.C. Iliuta, Sustainable production of high-purity hydrogen by sorption enhanced steam reforming of glycerol over CeO_2-promoted $Ca_9Al_6O_{18}$–CaO/NiO bifunctional material, ACS Sustain. Chem. Eng. 5 (2017) 9774–9786.
[71] M. Torimoto, Y. Sekine, Effects of alloying for steam or dry reforming of methane: a review of recent studies, Catal. Sci. Technol. 12 (2022) 3387–3411.
[72] H. Chen, S. Chansai, S. Xu, S. Xu, Y. Mu, C. Hardacre, X. Fan, Dry reforming of methane on bimetallic Pt–Ni@CeO_2 catalyst: a in situ DRIFTS-MS mechanistic study, Catal. Sci. Technol. 11 (2021) 5260–5272.
[73] N. Salvadó, S. Butí, E. Pantos, F. Bahrami, A. Labrador, T. Pradell, The use of combined synchrotron radiation micro FT-IR and XRD for the characterisation of Romanesque wall paintings, Appl. Phys. A 90 (2007) 67–73.
[74] H. Huang, Y. Yu, M. Zhang, Mechanistic insight into methane dry reforming over cobalt: a density functional theory study, Phys. Chem. Chem. Phys. 22 (2020) 27320–27331.
[75] Z. Osman, A.K. Arof, FTIR studies of chitosan acetate based polymer electrolytes, Electrochim. Acta 48 (2003) 993–999.
[76] J.-H. Kim, S.-B. Lee, S.Y. Kim, Incorporation effects of fluorinated side groups into polyimide membranes on their physical and gas permeation properties, J. Appl. Polym. Sci. 77 (2000) 2756–2767.
[77] Q. Zhuang, X. Si, L. Li, H. Zeng, Y. Ding, A self-adaptive multi-color fluorescent pH probe with the ability of whole cell imaging, Talanta 208 (2020), 119780.
[78] G. Athanasellis, O. Igglessi-Markopoulou, J. Markopoulos, Tetramic and tetronic acids as scaffolds in bioinorganic and bioorganic chemistry, Bioinorg. Chem. Appl. 2010 (2010), 315056.
[79] Y. Nabae, K.D. Pointon, J.T.S. Irvine, Ni/C slurries based on molten carbonates as a fuel for hybrid direct carbon fuel cells, J. Electrochem. Soc. 156 (2009) B716.
[80] D. Ochs, B. Braun, W. Maus-Friedrichs, V. Kempter, CO_2 chemisorption at Ca and CaO surfaces: a study with MIES, UPS(HeI) and XPS, Surf. Sci. 417 (1998) 406–414.
[81] B. Demri, D. Muster, XPS study of some calcium compounds, J. Mater. Process. Technol. 55 (1995) 311–314.
[82] P. Selvam, B. Viswanathan, V. Srinivasan, XPS studies of the surface properties of $CaNi_5$, J. Electron Spectrosc. Relat. Phenom. 49 (1989) 203–211.
[83] B. González, W. Liu, D.S. Sultan, J.S. Dennis, The effect of steam on a synthetic Ca-based sorbent for carbon capture, Chem. Eng. J. 285 (2016) 378–383.
[84] V. Materic, S.I. Smedley, High temperature carbonation of $Ca(OH)_2$, Ind. Eng. Chem. Res. 50 (2011) 5927–5932.

[85] Z.-H. Li, Y. Wang, K. Xu, J.-Z. Yang, S.-B. Niu, H. Yao, Effect of steam on CaO regeneration, carbonation and hydration reactions for CO_2 capture, Fuel Process. Technol. 151 (2016) 101–106.
[86] A. Wang, N. Deshpande, L.S. Fan, Steam hydration of calcium oxide for solid sorbent based CO_2 capture: effects of sintering and fluidized bed reactor behavior, Energy Fuel 29 (2014) 321–330.
[87] M. Fraune, U. Rüdiger, G. Güntherodt, S. Cardoso, P. Freitas, Size dependence of the exchange bias field in NiO/Ni nanostructures, Appl. Phys. Lett. 77 (2000) 3815–3817.